Evaluation of the hyperspectral radiometer (HSR1) at the ARM SGP site

Kelly A. Balmes[1, 2], Laura D. Riihimaki[1, 2], John Wood[3], Connor Flynn[4], Adam Theisen[5], Michael Ritsche[5], Lynn Ma[6], Gary B. Hodges[1, 2], Christian Herrera[1, 2]

5 [1]Cooperative Institute for Research in Environmental Sciences, University of Colorado Boulder, Boulder, CO, USA
[2]Global Monitoring Laboratory, National Oceanic and Atmospheric Administration (NOAA), Boulder, CO, USA
[3]Peak Design Ltd, Sunnybank House, Wensley Rd, Winster, Derbys, DE4 2DH, UK
[4]School of Meteorology, University of Oklahoma, Norman, OK, USA
[5]Argonne National Laboratory, Lemont, IL, USA
10 [6]Brookhaven National Laboratory, Upton, NY, USA

Correspondence to: Kelly A. Balmes (kelly.balmes@noaa.gov)

Abstract. The Peak Design Ltd hyperspectral radiometer (HSR1) was tested at the Atmospheric Radiation Measurement User Facility (ARM) Southern Great Plains (SGP) site in Lamont, Oklahoma for two months from May to July 2022. The HSR1 is a prototype instrument that measures total and diffuse spectral irradiance from 360 to 1100 nm with a spectral
15 resolution of 3 nm. The HSR1 spectral irradiance measurements are compared to nearby collocated spectral radiometers including two multifilter rotating shadowband radiometers (MFRSR) and a shortwave array spectroradiometer—hemispheric (SASHe). The total spectral irradiances at 500 nm for the HSR1 compared to the MFRSRs have a mean (relative) difference of 0.01 W m^{-2} nm^{-1} (1-2%). The HSR1 mean diffuse spectral irradiance at 500 nm is smaller than the MFRSRs by 0.03-0.04 (10%) W m^{-2} nm^{-1}. The HSR1 clear-sky aerosol optical depth (AOD) is also retrieved by considering Langley regressions
20 and compared to collocated instruments such as the Cimel sunphotometer (CSPHOT), MFRSRs, and SASHe. The mean HSR1 spectral AOD at 500 nm is larger than the CSPHOT by 0.010 (8%) and larger than the MFRSRs by 0.007-0.017 (6-18%). In general, good agreement between the HSR1 and other instruments is found in terms of the spectral total irradiance, diffuse irradiance, and AODs at 500 nm. The HSR1 quantities are also compared at other wavelengths to the collocated instruments, where similar agreement is found for the spectral irradiances, although relatively larger disagreement is found at
25 higher wavelengths, especially for spectral AODs.

1 Introduction

The shortwave (SW) radiation reaching the surface is dependent on the radiation incident at the top of the atmosphere (TOA) and the aerosols, clouds, and other atmospheric constituents that scatter, absorb, and extinguish the incoming radiation as it passes through the atmosphere. The surface downwelling SW radiation varies spatially, temporally,

30 and spectrally. By measuring the spectral SW radiation reaching the surface, insight into the physical, microphysical, and optical properties of aerosols and clouds are possible (Riihimaki et al., 2021).

Filter-based spectral SW radiation measurements have provided insight into the spectral characteristics of various atmospheric components by measuring at narrowband channels (Michalsky and Long, 2016; Riihimaki et al., 2021). For example, the multifilter rotating shadowband radiometers (MFRSR) (Harrison et al., 1994; Harrison and Michalsky, 1994;

35 Hodges and Michalsky, 2016) and Cimel sunphotometer (CSPHOT) (Holben et al., 1998; Giles et al., 2019) have increased knowledge on aerosols (e.g., McComiskey and Ferrare, 2016), clouds (e.g., Michalsky and Long, 2016; Min et al., 2008; Wang and Min, 2008), water vapor (e.g., Turner et al., 2016; Michalsky et al., 1995), and trace gases (e.g., Alexandrov et al., 2002a&b). In tandem with the increasing need for further understanding of aerosols and clouds to inform weather, climate, and renewable energy forecasting, spectral SW radiation measurements have advanced and hyperspectral radiometers are

40 more readily available. The Rotating Shadowband Spectrometer (RSS) (Harrison et al., 1999), Shortwave Array Spectroradiometer–Hemispheric (SASHe) (Flynn, 2016), and EKO MS-711 (García-Cabrera et al., 2020) are examples of existing hyperspectral radiometers. However, operations due to rotating shadowbands to measure the diffuse irradiance and calibrations of these instruments are challenging, as good solar alignment is needed for accurate measurements and moving parts have greater potential to fail in the field than stationary instrument components.

45 In an attempt to ease the operational difficulties of hyperspectral radiometry, a newly developed hyperspectral radiometer with no moving parts is now available called the hyperspectral radiometer (HSR1) (Wood et al., 2017; Norgren et al., 2022). The HSR1 measures total and diffuse spectral irradiance from 360 to 1100 nm with a spectral resolution of 3 nm. The total and diffuse irradiances are measured using a shadow pattern with seven sensors, which requires no moving parts or specific azimuthal alignment to separate the irradiance into components. With no moving parts, the instrument is ideal for

50 deployment on moving platforms such as ships and remote locations where regular maintenance is difficult. To make the instrument operate without moving parts, the HSR1 has a shadow pattern that follows the design of the Sunshine Pyranometer (SPN1) (Wood, 1999). The shadow pattern is described in Badosa et al. (2014) and Wood et al. (2017) (see their Figs. 1). Briefly, the shadow pattern allows one of the seven sensors to be illuminated unobstructed by the shadow pattern, which measures the total irradiance, and another sensor that measures half of the diffuse irradiance. As the sun

55 moves across the sky throughout the day, the sensor measuring the total irradiance and the sensor measuring the diffuse irradiance changes based on the sun and shadow pattern geometry. The diffuse irradiance is measured under the principle that half of the diffuse irradiance is measured in the minimum sensor at a given time. The measured diffuse assumes that the diffuse light is scattered equally angular, i.e., isotropic. The isotropic assumption may not be applicable due to the scattering properties of aerosols and clouds which may have a preferential scattering angle.

60 In this study, a prototype HSR1 is evaluated. The HSR1 was at the Atmospheric Radiation Measurement User Facility (ARM) Southern Great Plains (SGP) site in Lamont, Oklahoma for a two-month test period from May to July 2022. The ARM SGP site is an ideal location to evaluate a new instrument with the collocation of several instruments making similar measurements as a reference to compare with. The reference instruments include two MFRSRs, a CSPHOT, and a

Atmospheric
Measurement
Techniques

Discussions

SASHe utilized to evaluate the HSR1's ability to measure total spectral irradiance and diffuse spectral irradiances as well as

65   retrieve spectral aerosol optical depth (AOD).

Section 2 describes the HSR1 data and general performance as well as other instruments and data sources utilized in the evaluation. Section 3 details the HSR1 spectral AOD retrieval methodology. Section 4 presents the results of the HSR1 comparison. Section 5 briefly discusses post-processing modifications and calibration checks and the resultant implication on the HSR1 data and evaluation results. Section 6 summarizes and Sect. 7 presents concluding remarks.

70   **2 Data**

2.1 HSR1

The HSR1 prototype was at the ARM SGP site in Lamont, Oklahoma (36.61 °N, 97.49 °W) from 16 May 2022 to 18 July 2022 for the test period. The HSR1 was located on the guest instrument facility (GIF) at the Central Facility (C1). Data was collected and averaged to 1 min, which is the temporal resolution considered in this study. The HSR1 time period

75   sets the time period for the rest of the study. Other measurements (Sect. 2.2) are considered temporally collocated to the HSR1 when observations are within 1 min. The other instruments are considered spatially collocated to the HSR1, although the instruments are spatially distributed across the site. The collocated instruments are split between two facility designations C1 (36.607322 °N, 97.487643 °W) and E13 (36.604937 °N, 97.485561 °W).

Example time series for HSR1 integrated irradiance and example spectra from 28 June 2022 are shown in Fig. 1.

80   The integrated irradiance are the spectral irradiances integrated from 400 to 1000 nm. On this day, the conditions were primarily clear-sky. Other features of note in the time series and spectra from this day will be described throughout the remainder of this section.
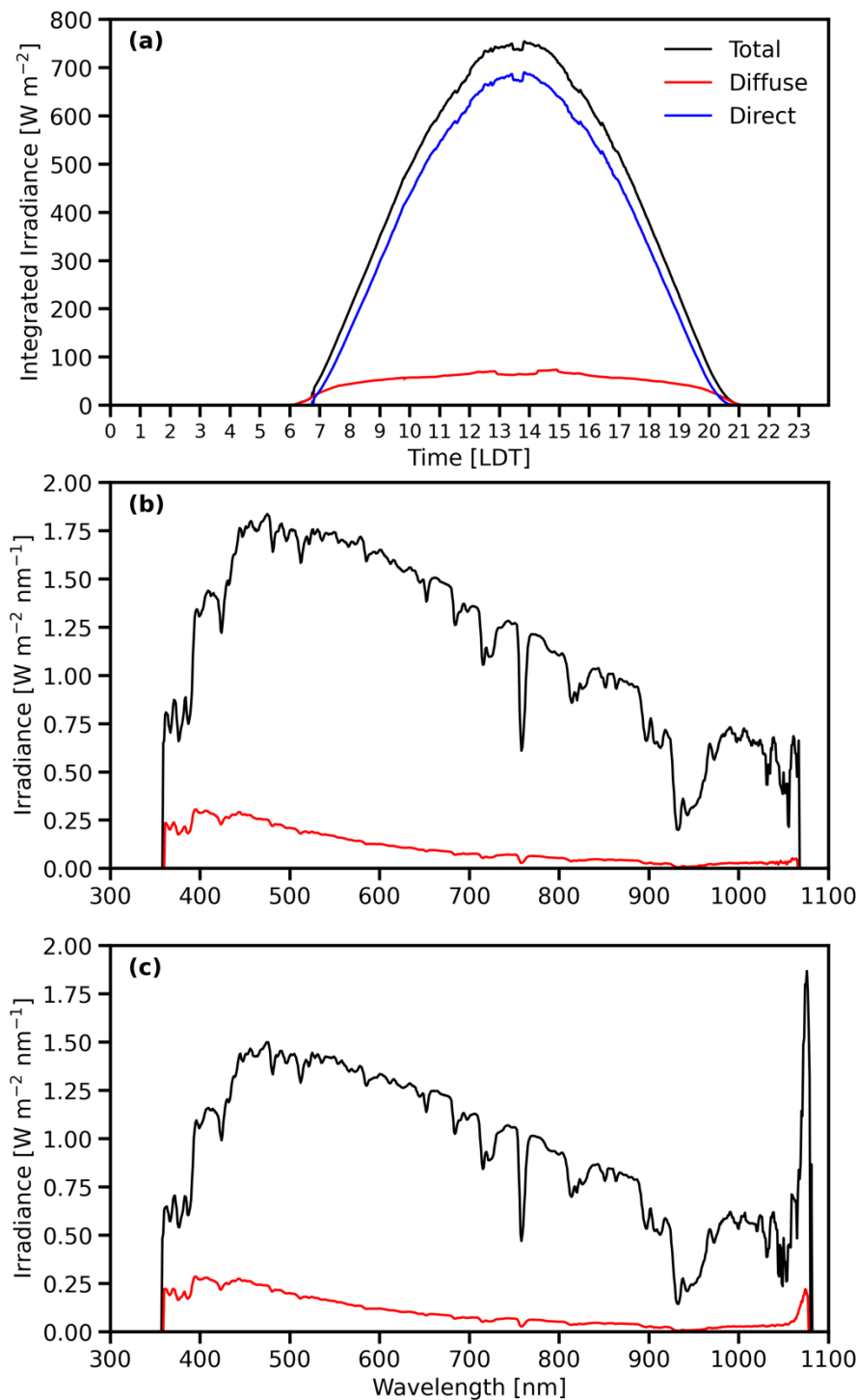
Figure 1: (a) HSR1 time series, in local daylight time (LDT), of integrated irradiance for total (black), diffuse (red), and direct (total - diffuse) (blue) irradiances from 28 June 2022. HSR1 spectra are from the same date at **(b)** 14:06 LDT and **(c)** 16:05 LDT.

The HSR1 operated autonomously with an uptime of 97.5% over the two-month test period. There were only two periods of downtime during the two months that were on the order of several hours. The first downtime period was related to a sitewide power outage from 11 June to 12 June. Excluding this sitewide outage, the HSR1 uptime was 98.9%. The second downtime period was related to data logging issues on 30 June. This downtime was possibly related to PC processing or software updates. The issue was partially remedied by reducing the data collection interval and the HSR1 collected data uninterrupted for the remainder of the test period. In addition, future designs of the HSR1 may improve upon computing performance as the instrument was constructed during a computer chip global supply chain shortage. As a result, improved computing performance may alleviate the brief downtime experienced by this specific prototype. Overall, the HSR1 exhibited excellent uptime and near-autonomous data collection over the two-month test period.

Beyond the HSR1 operability, several other features of the HSR1 performance were noted. The general excellent HSR1 performance is further described in later sections as the main focus of this study. Here, the limited performance issues are described. The data exhibited measurement noise due to straylight issues for wavelengths less than 400 nm and for wavelengths greater than 950 nm. In particular, considerable noise was noted for wavelengths greater than 1000 nm (Fig. 1c). Due to the measurement noise, this comparison study focuses on the spectral range of 400 to 950 nm. However, the HSR1 demonstrated the capability to measure total and diffuse spectral irradiance at wavelengths outside this spectral range (Figs. 1b&c). Future instrument design may overcome the current prototype's noise and the extended spectral range may be a high-quality measurable quantity in the future.

In addition to straylight issues, the data exhibited step functions throughout the diurnal cycle (Fig. 1a). This phenomenon is partially due to the shadow pattern design as the measurement switches between the seven sensors as the sun angle changes throughout the day. By utilizing seven sensors instead of one sensor, this introduces different calibration errors across the sensors that lead to the step functions. The HSR1 dome also contributes to this issue as the incoming light is bent due to the dome's refracting properties, which is referred to as the dome lensing effect. The dome lensing effect can be corrected for by a set of equations that take into account the geometry of the solar position and the HSR1 and the resultant change in angle of the incoming light as the light passes through the dome into the sensors. We consider how the dome lensing effect corrected total and diffuse spectral irradiances may affect the results in Sect. 5.

2.2 Other data

2.2.1 CSPHOT

The CSPHOT AODs are considered in the comparison (Holben et al., 1998). The CSPHOT observations are from the Aerosol Robotic Network (AERONET) Version 3 Level 2 AOD data product, which provides quality assured and filtered AODs during clear-sky conditions (Giles et al., 2019). The CSPHOT observations considered include the spectral AODs at 440, 500, 675, and 870 nm.

Atmospheric
Measurement
Techniques
Discussions

2.2.2 MFRSR

The multifilter rotating shadowband radiometer (MFRSR) measures narrowband total and diffuse spectral
120   irradiances at 415, 500, 615, 673, 870, and 940 nm (Harrison et al., 1994; Harrison and Michalsky, 1994; Hodges and
Michalsky, 2016). In addition to the spectral irradiances, MFRSR-retrieved spectral AODs are also considered at 415, 500,
615, 673, and 870 nm (Koontz et al., 2013). Two MFRSRs were collocated to the HSR1 with facility designations C1 and
E13.

2.2.3 SASHe

125   The Shortwave Array Spectroradiometer–Hemispheric (SASHe) measures total and diffuse spectral irradiances
from 300 to 1700 nm (Flynn, 2016). The spectral resolution is 2.4 nm from 300 to 1100 nm. Spectral AODs retrieved from
the SASHe generated by the instrument mentor are also considered. In this study, the SASHe clear-sky total spectral
irradiance, diffuse spectral irradiance, and spectral AODs at 415, 500, 615, 673, and 870 nm are compared to the other
instruments.

130   In the course of this study two data quality issues were identified affecting SASHe measurements. First, a
processing error was identified that yielded incorrect diffuse hemispheric and total irradiances. The measurements were
reprocessed by the mentor. For the diffuse irradiance, a factor of two correction was applied. The total irradiance was
recomputed as the sum of the direct and diffuse components. Second, mechanical play from a loose belt resulted in poor
shadowband separation of the direct and diffuse components. The mentor used the calibration independent ratio of direct
135   normal to diffuse hemispheric from the collocated MFRSRs (Sect. 2.2.2) as a reference to improve the SASHe separation of
direct and diffuse components. This approach requires clear-sky conditions and thus limits the SASHe irradiances to clear-
sky as well.

After these two data quality issues were addressed, the reprocessed SASHe measurements were calibrated via
Langley regressions in a similar manner to the MFRSRs and HSR1 (Sect. 3). AOD was retrieved from total optical depth by
140   subtracting contributions due to Rayleigh, ozone, and nitrogen dioxide for consistency with CSPHOT processing (Sect.
2.2.1).

2.2.4 Radflux

The Radiative Flux Analysis (Radflux) data product utilizes quality controlled broadband surface downwelling total
and diffuse shortwave (SW) irradiance observations to identify clear-sky periods and then calculate clear-sky irradiances
145   (Long and Ackerman, 2000; Long et al., 2006; Riihimaki et al., 2019). In this study, the clear-sky identified time periods
from Radflux (i.e., SW cloud fraction = 0) are considered for the AOD retrieval (Sect. 3). In addition, the broadband diffuse
ratio (i.e., diffuse/total) from Radflux are compared to those from the HSR1. The Radflux data product considered in this
study has the facility designation E13.

2.2.5 PAR

150   Photosynthetically active radiation (PAR), integrated total spectral irradiance from 400 to 700 nm, is measured by the PQS1 instrument as part of the Carbon Dioxide Flux Measurement System (CO2FLX) (Chan and Biraud, 2022). The measured PQS1 PAR is compared to the HSR1 PAR, which must first undergo a conversion to the same units as the PQS1. The HSR1 PAR is found by first converting the HSR1 total spectral irradiance from W m^{-2} to μmol m^{-2} s^{-1} by considering a spectral conversion factor (f) based on Planck's formula, such that:

155
$$f = \frac{\lambda}{hcN_a} \ x \ 10^{-3} \ = 0.00835935 \ \lambda \ , \tag{1}$$

where λ is the wavelength in nm, h is Planck's constant, c is the speed of light, and N_a is Avogadro's number. The spectral HSR1 in μmol m^{-2} s^{-1} is then integrated from 400 to 700 nm to obtain the HSR1 PAR.

2.2.6 Ozone satellite

     Ozone column amount for the AOD retrieval is from the ozone monitoring instrument (OMI) on board the Aura
160   satellite (Levelt et al., 2014). Global coverage at a spatial resolution of 1° latitude by 1° longitude of daily ozone values from OMI are provided in the gecomiX1.a1 data product. The daily ozone value corresponding to SGP's latitude and longitude are considered in the HSR1 AOD retrieval (Sect. 3).

3 AOD retrieval

     The HSR1 spectral AOD is retrieved by considering Langley regressions. The HSR1 AOD retrieval is based on the
165   AOD retrieval methodologies of the MFRSR (Koontz et al., 2013) and SASHe (Ermold et al., 2013). Only clear-sky periods are considered, which are based on the Radflux SW cloud fraction (Sect. 2.2.4). The spectral AOD are found for wavelengths with corresponding CSPHOT and MFRSR retrieved AODs: 415, 440, 500, 615, 673, 675, and 870 nm.

     For a clear-sky atmosphere (i.e., no clouds), the spectral direct normal irradiance (DNI) at a given wavelength (λ) that reaches the surface can be described as:

170
$$DNI(\lambda) = DNI_0(\lambda) exp \left[-\left(\tau_{Rayleigh} + \tau_{aerosol} + \tau_{gas} \right) m \right] , \tag{2}$$

where DNI_0 is the DNI at the top of the atmosphere (TOA), $\tau_{Rayleigh}$ is the Rayleigh optical depth due to molecular scattering, $\tau_{aerosol}$ is the AOD, τ_{gas} is the gaseous absorption optical depth, and m is the airmass. By considering the gaseous absorption as linearly proportional to the airmass and taking the natural logarithm, Eq. 2 becomes:

$$ln \left(DNI(\lambda) \right) = ln \left(DNI_0(\lambda) \right) - \left(\tau_{Rayleigh} + \tau_{aerosol} + \tau_{gas} \right) m \ . \tag{3}$$

175   By linearly regressing the HSR1 spectral DNI and airmass, the TOA DNI (from the y-intercept) and total optical depth (from the slope) can be found.

Atmospheric
Measurement
Techniques
Discussions

Besides DNI and AOD, the other terms in Eq. 3 are calculated as follows. The Rayleigh optical depth is calculated as (Hansen and Travis, 1974):

$$\tau_{Rayleigh} = \frac{p}{1013.25} 0.008569\lambda^{-4} \left(1 + 0.0133\lambda^{-2} + 0.00013\lambda^{-4}\right), \qquad (4)$$

180   where p is the surface pressure in mb, and λ is the wavelength in microns. The surface pressure considered is from Radflux. The airmass is calculated as (Kasten and Young, 1989):

$$m = \frac{1}{cos\left(\theta_s\right) + 0.50572\left(96.07995 - \theta_s\right)^{-1.6364}}, \qquad (5)$$

where θ_s is the solar zenith angle. For τ_{gas}, the ozone optical depth, τ_{ozone}, is considered and calculated as:

$$\tau_{ozone}(\lambda) = \frac{ozone\ columnar\ amount}{1000} x\ A_{ozone}(\lambda), \qquad (6)$$

185   where *ozone columnar amount* is the total amount of ozone in the atmospheric column in Dobson units and A_{ozone} is the spectrally-dependent ozone gas absorption coefficient. The ozone columnar amounts considered are from the daily ozone satellite value (Sect. 2.2.6) that are closest in time and the absorption coefficients considered are from Ermold et al. (2013) (see their Appendix A). Note that water vapor is not considered in τ_{gas} due to the wavelengths considered, which have a negligible amount of water vapor absorption.

190   Langley regressions are found each day for two periods: morning and afternoon. The minimum in airmass (i.e., solar noon) separates each day's clear-sky times into morning and afternoon. The TOA DNI are then filtered by only considering the interquartile range (i.e., 25th-75th percentile) and smoothed by considering a Savitzky-Golay filter. The filtered and smoothed TOA DNI values for each wavelength considered are then utilized to retrieve the spectral HSR1 AOD for each clear-sky time.

195   **4 Results**

4.1 Irradiance comparison

The HSR1 total and diffuse spectral irradiances were collocated and compared to those from the MFRSR C1 and MFRSR E13. The resultant comparison at 500 nm for the total spectral irradiance is shown in Fig. 2 and for the diffuse spectral irradiance is shown in Fig. 3.
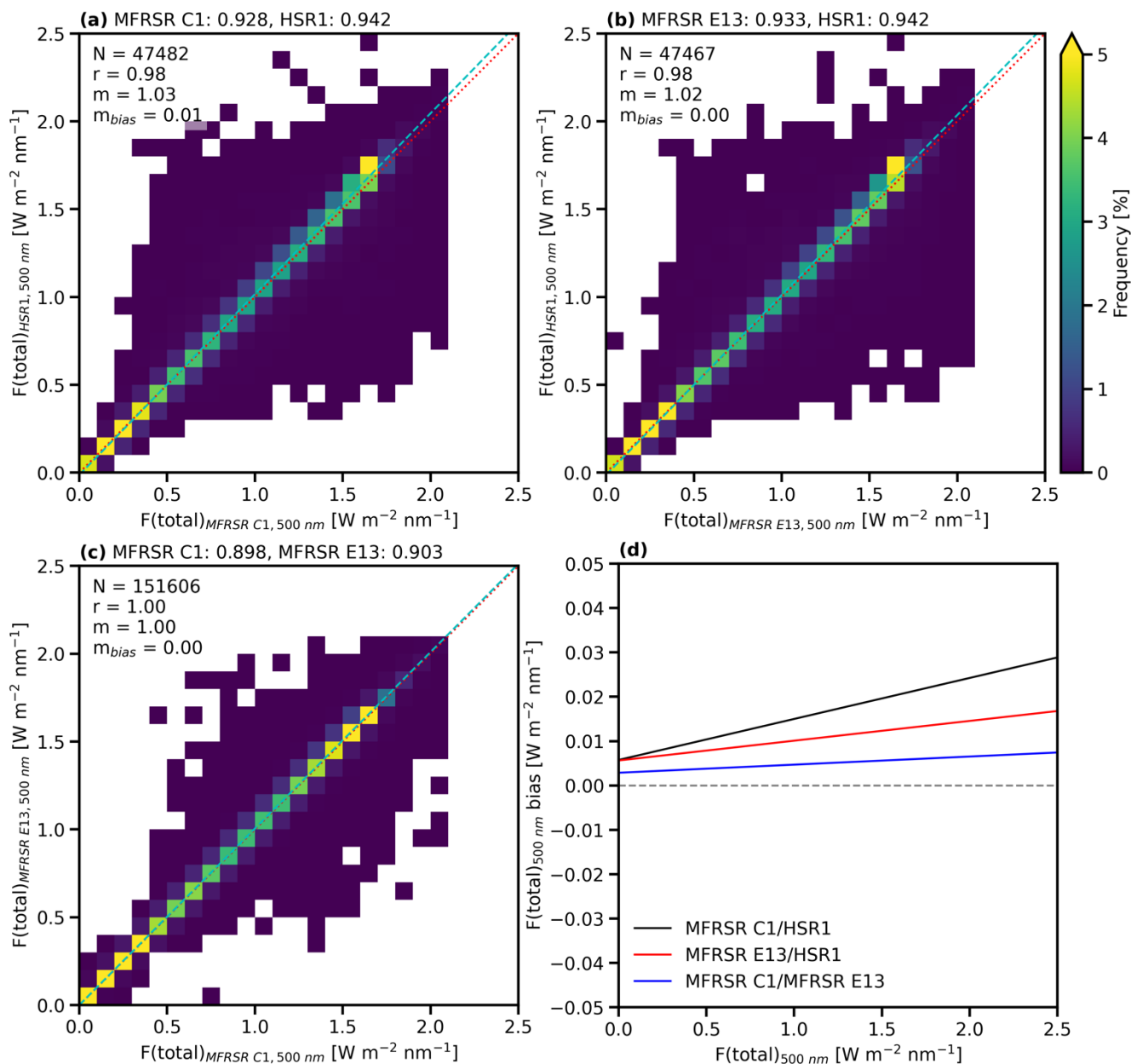
Figure 2: Frequency histogram for total spectral irradiance at 500 nm (W m^{-2} nm^{-1}) of collocated (a) MFRSR C1 and HSR1, (b) MFRSR E13 and HSR1, and (c) MFRSR C1and MFRSR E13. The mean values are given above each plot. The sample size (N), correlation coefficient (r), regression line slope (m), and bias regression line slope (m$_{bias}$) are shown in the top left of each plot. The 1:1 line is indicated by the dotted red line and the regression line is indicated by the dashed light blue line. (d) The regression lines of the bias are shown for MFRSR C1 and HSR1 (black), MFRSR E13 and HSR1 (red), and MFRSR C1 and MFRSR E13 (blue). The zero line is indicated by the dashed gray line.
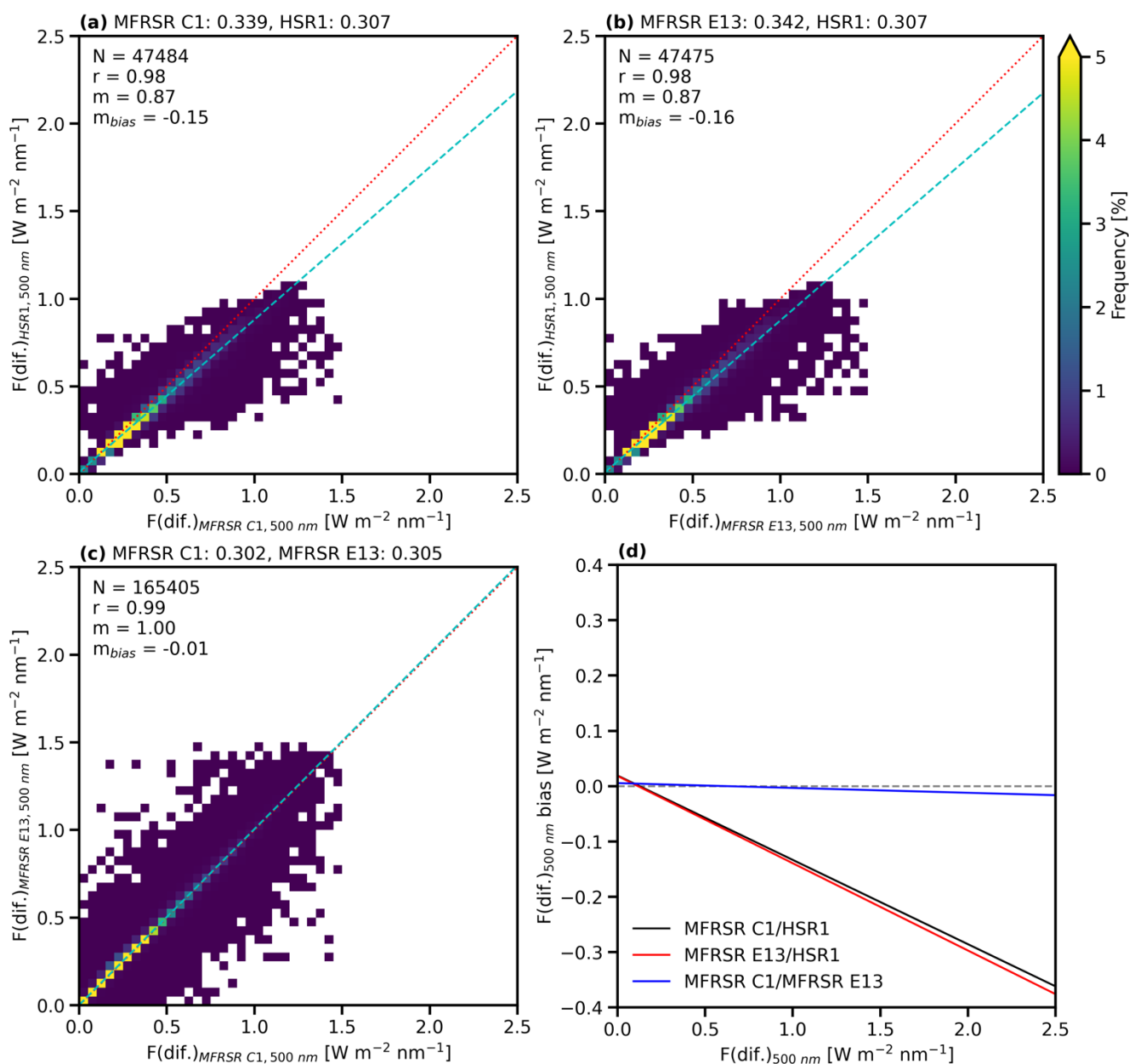
9

Atmospheric
Measurement
Techniques
Discussions

Figure 3: The same as Figure 2 but for diffuse spectral irradiance at 500 nm.

For the HSR1 total spectral irradiance at 500 nm, the mean (relative) differences compared to the MFRSR C1 and MFRSR E13 are 0.014 W m^{-2} nm^{-1} (1.5%) and 0.010 W m^{-2} nm^{-1} (1.1%). The total spectral irradiance correlation coefficients are 0.98 between the HSR1 and both MFRSRs. Orthogonal distance regressions were found for the comparisons as well as for the bias of the comparison. The regression slopes are 1.02-1.03 with bias regression slopes of 0.00-0.01. In

general, the HSR1 total spectral irradiance at 500 nm is slightly larger than those from both MFRSRs. However, the small

215   mean differences, large correlation coefficients, regression slopes near 1, and bias regression slopes near 0 demonstrate excellent agreement between the HSR1 and the two MFRSRs in terms of the total spectral irradiance at 500 nm.

For the HSR1 diffuse spectral irradiance at 500 nm, the mean (relative) differences compared to the MFRSR C1 and MFRSR E13 are -0.033 W m^{-2} nm^{-1} (-9.6%) and -0.036 W m^{-2} nm^{-1} (-10.4%). The diffuse spectral irradiance correlation coefficients are 0.98 between the HSR1 and both MFRSRs. The diffuse spectral irradiance regression slopes are 0.87

220   between the HSR1 and both MFRSRs with negative bias regression slopes of -0.15 (MFRSR C1) and -0.16 (MFRSR E13), which is further indicative of the smaller HSR1 diffuse irradiance compared to those from the MFRSRs. The relative differences are within about 10% indicating good agreement between the HSR1 and the MFRSRs in regards to the diffuse spectral irradiance at 500 nm. The HSR1 diffuse spectral irradiance is smaller than those from both MFRSRs, which may be partially related to the instrument design in how the HSR1 measures the diffuse irradiance as noted previously (Badosa et al.,

225   2014). The HSR1 also has a wider field of view (FOV) than the other instruments, so some of the forward-scattered circumsolar radiation is included in the direct fraction. Therefore, portions of the surface downwelling diffuse light are not measured by the HSR1 and may explain the underestimation observed in this comparison study.

The MFRSR C1 and MFRSR E13 were also compared in terms of the total and diffuse spectral irradiances at 500 nm and found to agree well. The mean (relative) difference in the total and diffuse spectral irradiance is 0.005 W m^{-2} nm^{-1}

230   (0.5%) and 0.003 W m^{-2} nm^{-1} (0.9%), respectively. The total and diffuse spectral irradiance correlation coefficients are also large: 1.00 (total) and 0.99 (diffuse). The regression slopes are also 1.00 for both total and diffuse spectral irradiance with bias regression slopes of 0.00 (total) and -0.01 (diffuse). The comparison of the spectral irradiances between the two MFRSRs with the same instrument design and same data processing quantifies some of the uncertainty. It is also encouraging for the HSR1 spectral irradiance comparison with an independent instrument design and data processing that the

235   HSR1 spectral irradiances agree well with those from the MFRSRs.

The HSR1 mean total and diffuse spectral irradiances were compared to the mean spectral irradiances from the MFRSRs for MFRSR wavelengths (i.e., 415, 500, 615, 673, 870, and 940 nm) in Fig. 4. The correlation coefficients, slope of the orthogonal distance regression, and slope of the orthogonal distance regression of the bias for the total and diffuse spectral irradiance comparison are provided in Table 1, Table 2, and Table 3, respectively. For the total spectral irradiance,

240   the results are similar to those at 500 nm (Fig. 2): the mean HSR1 total spectral irradiance is slightly larger than those from the MFRSRs. The exception is at 415 nm where the HSR1 total spectral irradiance is slightly smaller than those from the MFRSRs by 1.9% (MFRSR C1) to 2.6% (MFRSR E13). The relative differences between the HSR1 and the MFRSRs total spectral irradiances are 8% or less except at 940 nm where the HSR1 total spectral irradiance is larger than the MFRSRs by 21.0% (MFRSR C1) and 15.9% (MFRSR E13). The larger relative difference is partially due to the small magnitude of the

245   mean total spectral irradiance at 940 nm of 0.098-0.119 W m^{-2} nm^{-1} noting that the mean differences are 0.016-0.021 W m^{-2} nm^{-1}. For reference, the MFRSR C1 and MFRSR E13 total spectral irradiance comparison at 940 nm is the largest relative difference spectrally as well with 4.5%, which is considerably higher than other wavelengths where the relative differences

Atmospheric
Measurement
Techniques
Discussions

only ranged from 0.3 to 1.0%. This highlights the difficult and highly variable nature in measuring the total spectral irradiance at 940 nm where water vapor absorption is strong (Michalsky et al., 1995).

250
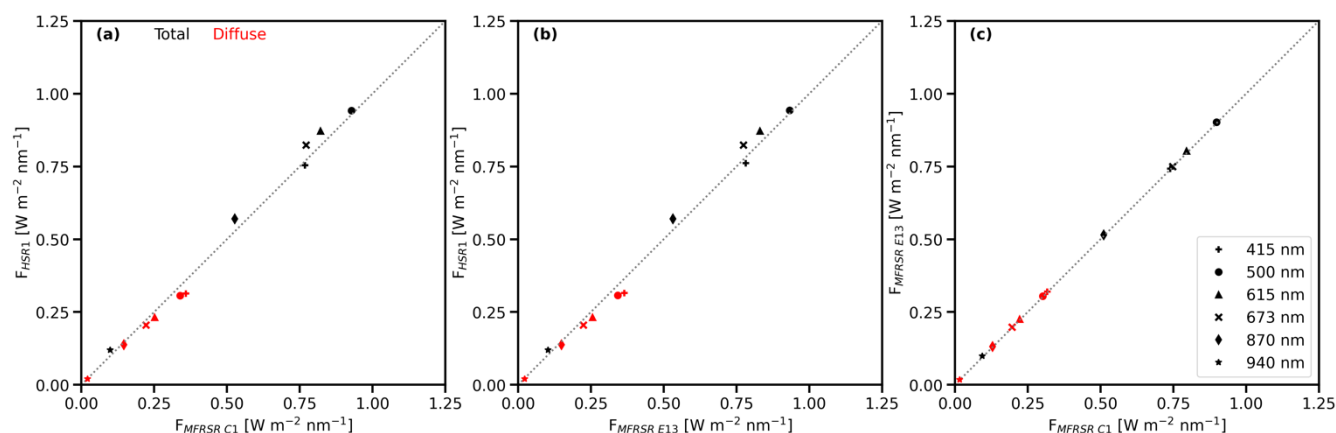
Figure 4: Mean total (black) and diffuse (red) spectral irradiances (W m^{-2} nm^{-1}) of collocated (a) MFRSR C1 and HSR1, (b) MFRSR E13 and HSR1, and (c) MFRSR C1 and MFRSR E13. The wavelengths considered include 415 (plus sign), 500 (circle), 615 (triangle), 673 (x-mark), 870 (diamond), and 940 (star) nm. The 1:1 line is indicated by the dotted gray line.

255 **Table 1. The correlation coefficients for the (top) total spectral irradiance, (middle) diffuse spectral irradiance, and (bottom) spectral AOD at corresponding wavelengths (i.e., 415, 440, 500, 615, 673, 675, 870, and 940 nm). The values correspond to collocated times between the HSR1, CSPHOT, MFRSR C1, MFRSR E13, and clear-sky SASHe (left column).**

	Wavelength (nm)							
Total Spectral Irradiance	415	440	500	615	673	675	870	940
MFRSR C1 & HSR1	0.99	--	0.98	0.98	0.98	--	0.97	0.98
MFRSR E13 & HSR1	0.99	--	0.98	0.98	0.98	--	0.97	0.98
SASHe & HSR1	0.99	--	0.98	0.98	0.97	--	0.97	--
MFRSR C1 & MFRSR E13	1.00	--	1.00	1.00	1.00	--	1.00	1.00
MFRSR C1 & SASHe	0.99	--	0.98	0.98	0.97	--	0.97	--
MFRSR E13 & SASHe	0.99	--	0.98	0.98	0.97	--	0.97	--

Diffuse Spectral Irradiance	415	440	500	615	673	675	870	940
MFRSR C1 & HSR1	0.98	--	0.98	0.97	0.97	--	0.97	0.96
MFRSR E13 & HSR1	0.98	--	0.98	0.97	0.97	--	0.97	0.96
SASHe & HSR1	0.98	--	0.97	0.97	0.95	--	0.97	--
MFRSR C1 & MFRSR E13	0.99	--	0.99	0.99	0.98	--	0.99	0.98
MFRSR C1 & SASHe	0.97	--	0.95	0.94	0.92	--	0.94	--

Atmospheric
Measurement
Techniques
Discussions

Open Access

EGU

MFRSR E13 & SASHe	0.99	--	0.98	0.98	0.97	--	0.97	--

Spectral AOD	415	440	500	615	673	675	870	940
MFRSR C1 & HSR1	0.94	--	0.91	0.82	0.79	--	0.67	--
MFRSR E13 & HSR1	0.94	--	0.92	0.83	0.81	--	0.61	--
SASHe & HSR1	0.97	--	0.94	0.88	0.86	--	0.74	--
CSPHOT & HSR1	--	0.95	0.94	--	--	0.86	0.75	--
MFRSR C1 & MFRSR E13	0.97	--	0.94	0.89	0.88	--	0.85	--
MFRSR C1 & SASHe	0.98	--	0.98	0.95	0.90	--	0.87	--
MFRSR E13 & SASHe	0.98	--	0.97	0.93	0.90	--	0.86	--
CSPHOT & MFRSR C1	--	--	0.97	--	--	--	0.91	--
CSPHOT & MFRSR E13	--	--	0.99	--	--	--	0.98	--
CSPHOT & SASHe	--	--	0.97	--	--	--	0.87	--

Table 2. The same as Table 1 but for the regression line slope.

	Wavelength (nm)							
Total Spectral Irradiance	415	440	500	615	673	675	870	940
MFRSR C1 & HSR1	0.99	--	1.03	1.07	1.07	--	1.09	1.25
MFRSR E13 & HSR1	0.98	--	1.02	1.06	1.07	--	1.08	1.20
SASHe & HSR1	1.01	--	1.06	1.09	1.14	--	1.14	--
MFRSR C1 & MFRSR E13	1.00	--	1.00	1.01	1.00	--	1.00	1.04
MFRSR C1 & SASHe	0.98	--	0.98	0.98	0.94	--	0.96	--
MFRSR E13 & SASHe	0.98	--	0.97	0.97	0.94	--	0.96	--

Diffuse Spectral Irradiance	415	440	500	615	673	675	870	940
MFRSR C1 & HSR1	0.85	--	0.87	0.89	0.89	--	0.91	1.01
MFRSR E13 & HSR1	0.84	--	0.87	0.88	0.89	--	0.91	0.98
SASHe & HSR1	0.89	--	0.90	0.90	0.92	--	0.94	--
MFRSR C1 & MFRSR E13	1.01	--	1.00	1.01	1.00	--	1.01	1.04
MFRSR C1 & SASHe	0.94	--	0.95	0.96	0.94	--	0.94	--
MFRSR E13 & SASHe	0.93	--	0.94	0.95	0.93	--	0.93	--

Spectral AOD	415	440	500	615	673	675	870	940

	415	440	500	615	673	675	870	940
MFRSR C1 & HSR1	0.94	--	0.95	0.99	1.03	--	1.01	--
MFRSR E13 & HSR1	0.99	--	1.02	1.09	1.18	--	1.22	--
CSPHOT & HSR1	--	0.89	0.88	--	--	0.89	0.81	--
SASHe & HSR1	0.90	--	0.90	0.92	0.88	--	0.65	--
MFRSR C1 & MFRSR E13	0.97	--	0.95	0.93	0.90	--	0.89	--
MFRSR C1 & SASHe	1.12	--	1.16	1.20	1.33	--	1.30	--
MFRSR E13 & SASHe	1.14	--	1.21	1.28	1.42	--	1.46	--
CSPHOT & MFRSR C1	--	--	0.93	--	--	--	0.94	--
CSPHOT & MFRSR E13	--	--	0.90	--	--	--	0.85	--
CSPHOT & SASHe	--	--	1.00	--	--	--	1.03	--

260

Table 3. The same as Table 1 but for the bias regression line slope.

	Wavelength (nm)							
Total Spectral Irradiance	415	440	500	615	673	675	870	940
MFRSR C1 & HSR1	-0.02	--	0.01	0.05	0.05	--	0.06	0.24
MFRSR E13 & HSR1	-0.03	--	0.00	0.03	0.05	--	0.05	0.18
SASHe & HSR1	0.00	--	0.04	0.07	0.12	--	0.11	--
MFRSR C1 & MFRSR E13	0.00	--	0.00	0.01	0.00	--	0.00	0.04
MFRSR C1 & SASHe	-0.03	--	-0.04	-0.04	-0.09	--	-0.07	--
MFRSR E13 & SASHe	-0.04	--	-0.04	-0.05	-0.09	--	-0.07	--
Diffuse Spectral Irradiance	415	440	500	615	673	675	870	940
MFRSR C1 & HSR1	-0.17	--	-0.15	-0.14	-0.14	--	-0.11	-0.03
MFRSR E13 & HSR1	-0.17	--	-0.16	-0.15	-0.14	--	-0.12	-0.07
SASHe & HSR1	-0.13	--	-0.13	-0.13	-0.14	--	-0.09	--
MFRSR C1 & MFRSR E13	0.00	--	-0.01	0.00	-0.01	--	-0.01	0.02
MFRSR C1 & SASHe	-0.09	--	-0.11	-0.10	-0.15	--	-0.12	--
MFRSR E13 & SASHe	-0.10	--	-0.12	-0.12	-0.16	--	-0.14	--
Spectral AOD	415	440	500	615	673	675	870	940
MFRSR C1 & HSR1	-0.12	--	-0.15	-0.26	-0.31	--	-0.60	--
MFRSR E13 & HSR1	-0.08	--	-0.08	-0.17	-0.14	--	-0.84	--
CSPHOT & HSR1	--	-0.16	-0.18	--	--	-0.28	-0.49	--

Atmospheric
Measurement
Techniques
Open Access
Discussions
EGU

SASHe & HSR1	-0.13	--	-0.16	-0.22	-0.29	--	-0.57	--
MFRSR C1 & MFRSR E13	-0.07	--	-0.11	-0.20	-0.24	--	-0.29	--
MFRSR C1 & SASHe	0.10	--	0.14	0.16	0.23	--	0.15	--
MFRSR E13 & SASHe	0.12	--	0.18	0.21	0.35	--	0.37	--
CSPHOT & MFRSR C1	--	--	-0.10	--	--	--	-0.16	--
CSPHOT & MFRSR E13	--	--	-0.10	--	--	--	-0.16	--
CSPHOT & SASHe	--	--	-0.03	--	--	--	-0.14	--

Similar to the total spectral irradiance comparison described above, the diffuse spectral irradiance comparison at all
265   MFRSR wavelengths is also similar to the comparison at 500 nm (Fig. 3): the HSR1 diffuse spectral irradiances are smaller than those from both the MFRSRs at all MFRSR wavelengths by ~4-14%. The relative differences range from -3.7% for the HSR1 diffuse spectral irradiance compared to those from the MFRSR C1 at 940 nm to -13.5% for the HSR1 diffuse spectral irradiance compared to those from the MFRSR E13 at 415 nm. Interestingly, the mean diffuse spectral irradiance for the HSR1 compared to those from the MFRSR C1 at 940 nm agree better than the MFRSR C1 and MFRSR E13 diffuse spectral
270   irradiances at 940 nm (9.8%). However, the mean differences for the diffuse spectral irradiance at 940 nm are only 0.001-0.003 W m^{-2} nm^{-1}. Similar to the total spectral irradiance, the MFRSR C1 and MFRSR E13 diffuse spectral irradiance comparison at 940 nm is the largest relative difference, which is nearly an order of magnitude larger than all other wavelengths (0.9-1.9%). This further highlights the challenges in measuring the spectral irradiance at 940 nm.

The impact of the MFRSR filter on the comparison results were considered. The HSR1 spectral measurements are
275   at a spectral resolution of 3 nm, whereas the MFRSR filters measure with a nominal central wavelength at each desired wavelength and a nominal full width half maximum (FWHM) of 10 nm. In reality, the MFRSR filter has a measured central wavelength and a measured FWHM for each narrowband channel that represents the transmission characteristics of each specific instrument. For example, the MFRSR C1 measured characteristics for the 500 nm channel includes a central wavelength of 501.5 nm and a FWHM of 10.7 nm. Here we assess the impact of the MFRSR filter on the comparison results
280   by considering the HSR1 spectra weighted by the MFRSR transmission spectra. In general, the HSR1 mean spectral irradiances decreased with the mean total spectral irradiance decreasing by 0.012 W m^{-2} nm^{-1} or less and the mean diffuse spectral irradiance decreasing by 0.005 W m^{-2} nm^{-1} or less. This resulted in the mean total spectral irradiance comparison between the HSR1 and the two MFRSRs improving by 0.1-1.0%, except at 940 nm where it improved by ~2.5% and at 415 nm where it worsened by 1.0-1.5%. For the mean diffuse spectral irradiances, the comparison worsened by 1.5% or less
285   except at 940 nm where it worsened by ~3.5%. Overall, the impact of the MFRSR filter is minimal on the results with changes in the HSR1 spectral irradiances and resultant comparison by ~0.01 W m^{-2} nm^{-1} (~1.5%) or less on average.

15

Atmospheric
Measurement
Techniques
Discussions

### 4.1.1 SASHe clear-sky irradiance comparison

The HSR1 total and diffuse spectral irradiances were collocated and compared to the SASHe clear-sky irradiances. The SASHe clear-sky irradiances were also compared to the two MFRSRs. The resultant comparison for the total and diffuse spectral irradiances are shown in Fig. 5.

For the total spectral irradiance at 500 nm (Fig. 5a), the mean (relative) difference for the HSR1 total spectral irradiance compared to those from the SASHe is 0.017 W m^{-2} nm^{-1} (1.5%). The correlation coefficient is 0.98 with a regression slope of 1.06 and bias regression slope of 0.04, which further suggests that the HSR1 total spectral irradiance is larger than those from the SASHe. The SASHe total spectral irradiance were also compared to those from the two MFRSRs (Figs. 5b&c). The mean (relative) differences for the SASHe total spectral irradiance compared to those from the MFRSR C1 and MFRSR E13 are 0.004 W m^{-2} nm^{-1} (0.4%) and -0.001 W m^{-2} nm^{-1} (-0.1%) with correlation coefficients of 0.98. The regression slopes are less than 1 (0.97-0.98) and the bias regression slopes are negative (-0.04), which is due to biased low SASHe total spectral irradiance values at larger irradiance values (>~1.5 W m^{-2} nm^{-1}).

For the diffuse spectral irradiance at 500 nm, the mean (relative) difference for the HSR1 diffuse spectral irradiance compared to those from the SASHe is -0.019 W m^{-2} nm^{-1} (-6.4%). Similar to the HSR1 comparison in Fig. 3, the HSR1 diffuse spectral irradiance is smaller than those from the SASHe. The SASHe diffuse spectral irradiance is slightly smaller than those from the MFRSRs by -0.007 W m^{-2} nm^{-1} (-2.5%) and -0.011 W m^{-2} nm^{-1} (-3.6%) for the MFRSR C1 and MFRSR E13, respectively.

The mean total and diffuse spectral irradiances were compared to the mean spectral irradiances between the SASHe and HSR1 (Fig. 5i), MFRSR C1 and SASHe (Fig. 5j), and MFRSR E13 and SASHe (Fig. 5k) at 415, 500, 615, 673, and 870 nm. The SASHe and HSR1 mean total spectral irradiance comparison are similar to those at 500 nm as the HSR1 total spectral irradiance is typically slightly larger than those from the SASHe by 0.08 W m^{-2} nm^{-1} (9%) or less except at 415 nm where the HSR1 total spectral irradiance is smaller by 0.01 W m^{-2} nm^{-1} (1.5%). The SASHe mean spectral irradiances compared to those from the two MFRSRs agree within 2% or less for all wavelengths. For the diffuse mean spectral irradiance comparison, the HSR1 diffuse spectral irradiance is smaller than those from the SASHe by 0.03 W m^{-2} nm^{-1} (9%) or less. The SASHe mean diffuse spectral irradiances compared to those from the MFRSRs are smaller by 0.02 W m^{-2} nm^{-1} or less. This corresponds to within 5% or less except at 673 and 870 nm where the relative differences are within 5-8%.
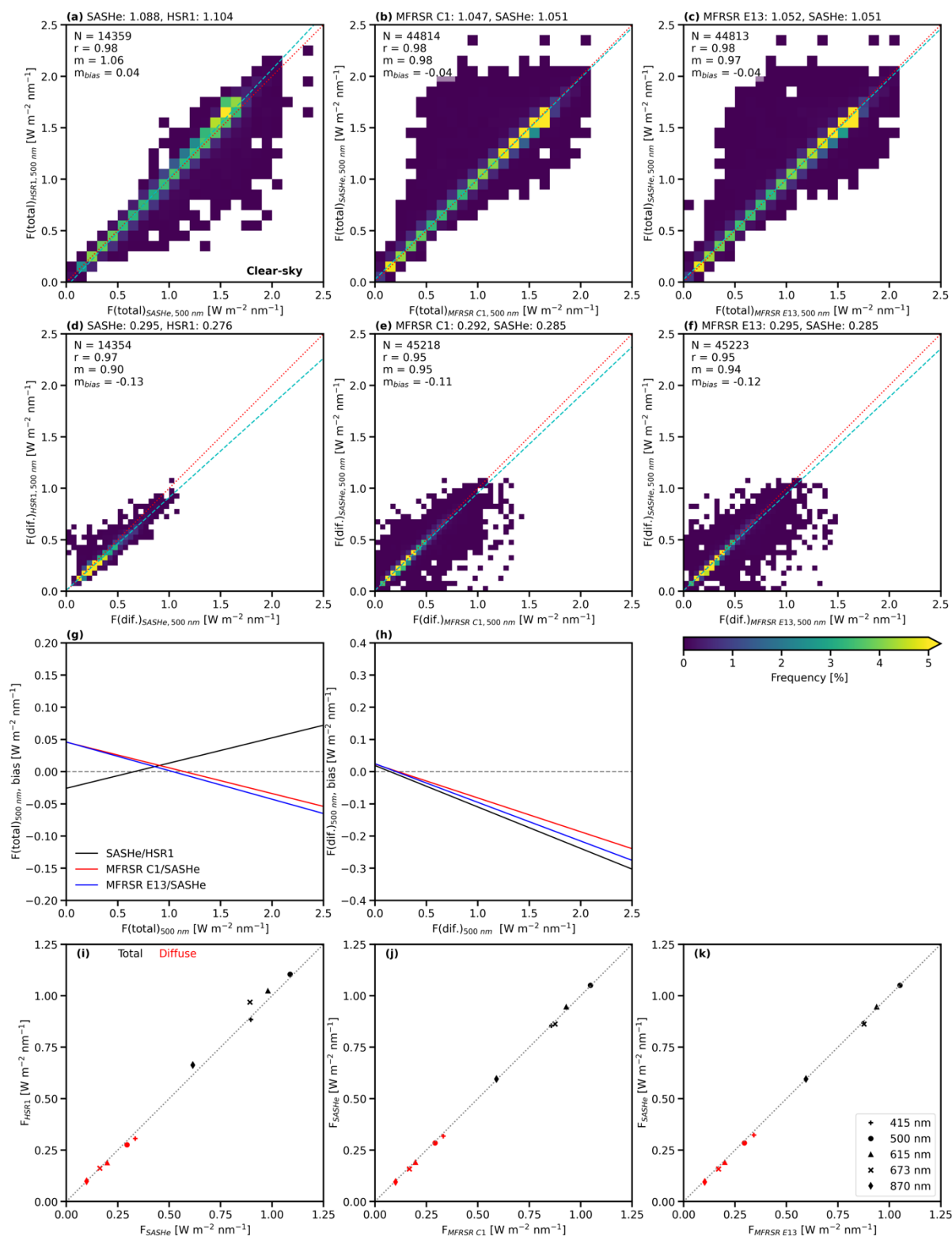
Figure 5: Frequency histogram for (a-c) total and (d-f) diffuse clear-sky spectral irradiance at 500 nm (W m^{-2} nm^{-1}) of collocated (left) SASHe and HSR1, (center) MFRSR C1 and SASHe, and (right) MFRSR E13 and SASHe. The mean values are given above each plot. The sample size (N), correlation coefficient (r), regression line slope (m), and bias regression line slope (m$_{bias}$) are shown in the top left of each plot. The 1:1 line is indicated by the dotted red line and the regression line is indicated by the dashed light blue line. The regression lines of the (g) total and (h) diffuse spectral irradiance bias are shown for SASHe and HSR1 (black), MFRSR C1 and SASHe (red), and MFRSR E13 and SASHe (blue). The zero line is indicated by the dashed gray line. (i-k) The mean total (black) and diffuse (red) clear-sky spectral irradiance of collocated (left) SASHe and HSR1, (center) MFRSR C1 and SASHe, and (right) MFRSR E13 and SASHe at 415 (plus sign), 500 (circle), 615 (triangle), 673 (x-mark), and 870 (diamond) nm. The 1:1 line is indicated by the dotted gray line.

4.2 AOD comparison

The HSR1 clear-sky spectral AODs were collocated and compared to those from the CSPHOT, two MFRSRs, and SASHe. The resultant comparison of the AODs at 500 nm is shown in Fig. 6. For the HSR1 spectral AOD at 500 nm, the mean (relative) differences compared to those from the CSPHOT, MFRSR C1, MFRSR E13, and SASHe are 0.010 (8.0%), 0.007 (6.4%), 0.017 (17.7%), and -0.008 (-6.2%), respectively. The correlation coefficients are 0.94, 0.91, 0.92, and 0.94 for the HSR1 AOD comparison to those from the CSPHOT, MFRSR C1, MFRSR E13, and SASHe, respectively. The regression slopes are 0.88, 0.95, 1.02, and 0.90 between the HSR1 and CSPHOT, MFRSR C1, MFRSR E13, and SASHe, respectively. The regression slopes of the bias are -0.18, -0.15, -0.08, and -0.16 between the HSR1 AODs and those from the CSPHOT, MFRSR C1, MFRSR E13, and SASHe, respectively. With regression slopes less than 1 and negative slopes for the bias, this highlights that the HSR1 AOD is typically biased high at smaller AODs (~0.05-0.10) except for the SASHe AOD where the HSR1 AOD is biased low at larger AODs (~0.30-0.40).

In general, the HSR1 AOD is larger than those from the other instruments except for those from the SASHe. Besides the MFRSR E13 AODs, the mean differences are 0.01 or less with less than 10% relative differences, demonstrating excellent agreement in the spectral AOD at 500 nm between the HSR1 AOD and the CSPHOT, MFRSR C1, and SASHe AODs. In particular, the mean difference of 0.010 between the CSPHOT AOD and HSR1 AOD is encouraging, noting that the CSPHOT AOD uncertainty is 0.01 (Giles et al., 2019).

The CSPHOT, MFRSR C1, MFRSR E13, and SASHe AODs were also compared for spectral AOD at 500 nm and found to agree well. For the CSPHOT AOD comparison, the mean (relative) difference with the MFRSR C1, MFRSR E13, and SASHe AODs are 0.007 (7.5%), -0.004 (-4.4%), and 0.014 (10.0%), respectively. The mean (relative) difference in AODs between the MFRSR C1 and MFRSR E13, MFRSR C1 and SASHe, and MFRSR E13 and SASHe is -0.010 (-9.8%), 0.002 (2.3%), and 0.012 (12.0%), respectively. The correlation coefficients are also large, ranging from 0.94 to 0.99. The regression slopes are near 1 ranging from 0.90 to 1.00 except for the MFRSRs AODs compared to the SASHe AODs which are 1.16 and 1.21. The regression slopes of the bias are negative with values of -0.11 or less, except for the MFRSRs AODs compared to the SASHe AODs where the bias slope is positive with values of 0.14 and 0.18. Similar to the total and diffuse spectral irradiance comparison, the MFRSR C1 and MFRSR E13 AOD comparison slightly disagree and that disagreement provides insight into part of the uncertainty of the measurement and AOD retrieval methods. The HSR1 AOD agrees with

350   those from the other instruments, which is encouraging that some of the disagreement could be related to uncertainty inherent in the measurement and methods.

Atmospheric
Measurement
Techniques
Discussions
Open Access
EGU
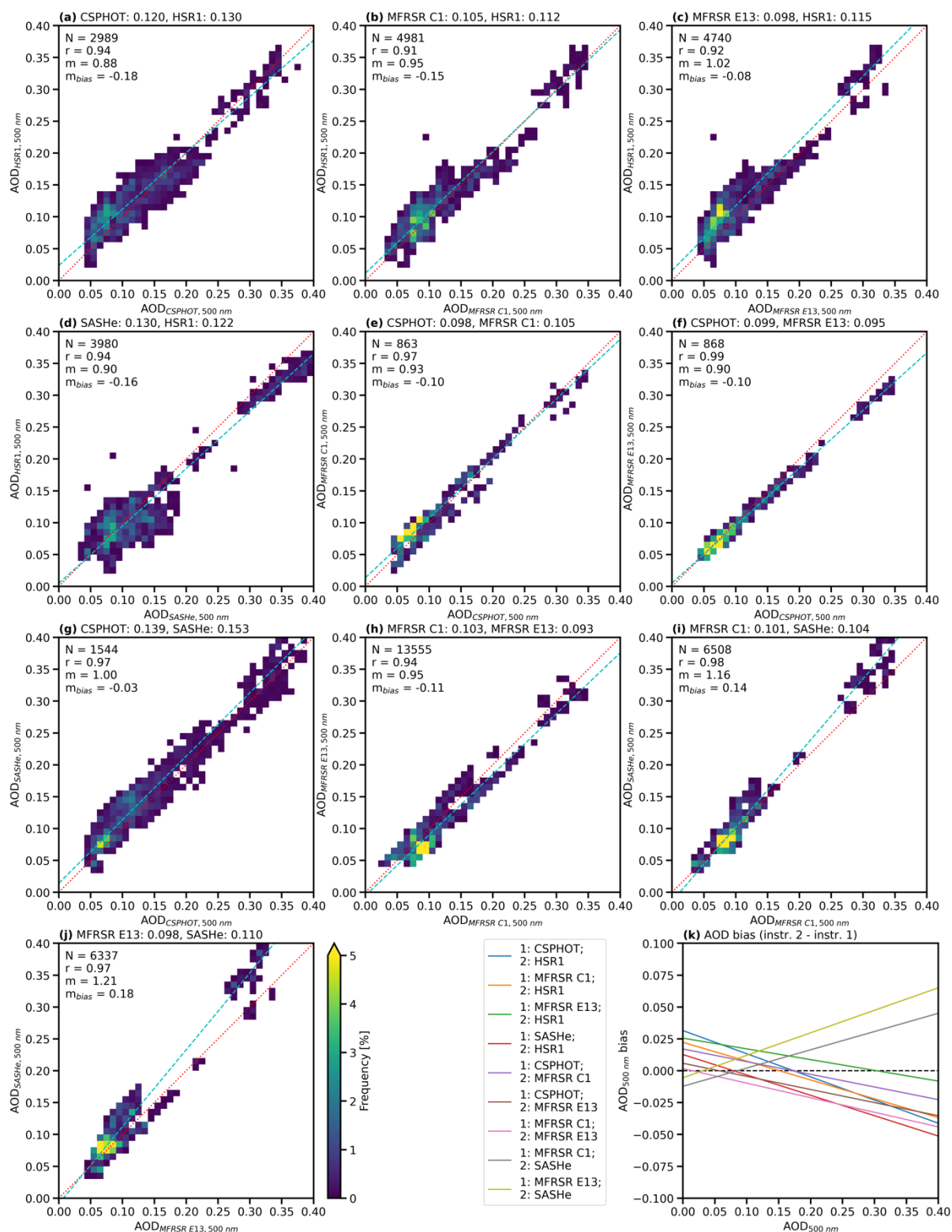
Figure 6: Frequency histogram for AOD at 500 nm of collocated (a) CSPHOT and HSR1, (b) MFRSR C1 and HSR1, (c) MFRSR E13 and HSR1, (d) SASHe and HSR1, (e) CSPHOT and MFRSR C1, (f) CSPHOT and MFRSR E13, (g) CSPHOT and SASHe, (h) MFRSR C1 and MFRSR E13, (i) MFRSR C1 and SASHe, and (j) MFRSR E13 and SASHe. The mean values are given above each plot. The sample size (N), correlation coefficient (r), slope of the regression line (m), and slope of the regression line of the bias (m$_{bias}$) are shown in the top left of each plot. The 1:1 line is indicated by the dotted red line and the regression line is indicated by the dashed light blue line. (k) The regression lines of the bias are shown for each instrument comparison where the reference instrument (1) is compared to another instrument (2). The zero line is indicated by the dashed black line.

The HSR1 mean clear-sky spectral AODs were compared to mean spectral AODs from the CSPHOT, MFRSRs, and SASHe for overlapping wavelengths (i.e., 415, 440, 500, 615, 673, 675, and 870 nm) in Fig. 7. The spectral AOD results at all wavelengths are similar to those at 500 nm (Fig. 6): the mean HSR1 AOD is larger than those from the CSPHOT and the two MFRSRs except for the mean SASHe AOD, which is larger than the mean HSR1 AOD. The only spectral range where the HSR1 AOD is smaller than those from all other instruments is at 415 nm (MFRSRs and SASHe) and 440 nm (CSPHOT). The mean spectral HSR1 AOD for the 415 and 440 nm channels is smaller than those from the CSPHOT, MFRSR C1, MFRSR E13, and SASHe by 8.2%, 21.8%, 14.4%, and 23.1%. For 440 and 500 nm, the mean spectral HSR1 AOD comparison to the mean spectral CSPHOT AOD are within ~8% and ~0.01. However, the disagreement in the 675 and 870 nm AOD comparisons are larger: 0.021 (25.8%) and 0.030 (46.9%), respectively. For the MFRSRs AOD, better agreement is found between the HSR1 and MFRSR C1 AODs than between the HSR1 and MFRSR E13 AODs. The relative differences between the mean spectral HSR1 AOD and MFRSR C1 AOD are 25% or less except for at 870 nm where it is 38.0%. In contrast, the relative differences between the mean spectral HSR1 AOD and MFRSR E13 AOD is 14-18% for smaller wavelengths (i.e., 415 and 500 nm) but 35-66% for larger wavelengths (i.e., 615, 673, and 870 nm). For the SASHe AOD, the HSR1 AOD is smaller by 10% or less except at 415 nm where the HSR1 AOD is smaller by 23.1% and 870 nm where the HSR1 is larger by 32.4%. The correlation coefficients are generally higher for smaller relative differences and are generally lower for larger relative differences in AOD (Table 1). For example, the correlation coefficients are 0.91-0.95 for 415 and 500 nm but 0.61-0.86 for the 615, 673, and 870 nm HSR1 AOD comparisons. Similarly, the regression slopes are closer to 1 and the regression slopes of the bias are closer to 0 for smaller relative differences and the opposite is seen for larger relative differences. For example, the regression slopes range from 0.65 to 1.22 for the 870 nm HSR1 AOD comparisons. Furthermore, the bias regression slopes are within ~0.2-0.3 except for 870 nm where the slopes range from -0.49 to -0.84.

The mean spectral CSPHOT AOD were compared to the two MFRSRs and SASHe AODs at the two overlapping wavelengths (i.e., 500 and 870 nm) and the mean AODs are largely found to agree well. The AOD comparison at 500 nm is described above. For 870 nm, the mean (relative) difference between the CSPHOT AOD with those from the MFRSR C1, MFRSR E13, and SASHe is 0.009 (18.3%), -0.002 (-3.5%), and 0.04 (6.0%), respectively. The correlation coefficients (Table 1) are also large between the CSPHOT AOD and those from the other instruments: 0.91 (MFRSR C1), 0.98 (MFRSR E13), and 0.87 (SASHe). The regression slopes are slightly further from 1 and the bias regression slopes are more negative for the 870 nm AOD comparison, noting that the regression slope range is 0.85 to 1.03 and the bias regression slope range is

-0.14 to -0.16. The AODs from the two MFRSRs are compared to each other as well. The mean differences are all 0.009-

390   0.011 with relative differences of 8-17%. The MFRSRs and the SASHe AODs were also compared to each other. The

SASHe AOD is typically larger than those from the two MFRSRs ranging from a relative difference of 2% to up to 41% at

615 nm. The exception is when the SASHe AOD is smaller than the MFRSR AOD which includes at 940 nm and for the

MFRSR C1 AOD at 415 nm. In general, better agreement is found between the other instruments AODs besides the HSR1

AOD, which is particularly the case at larger wavelengths.

395
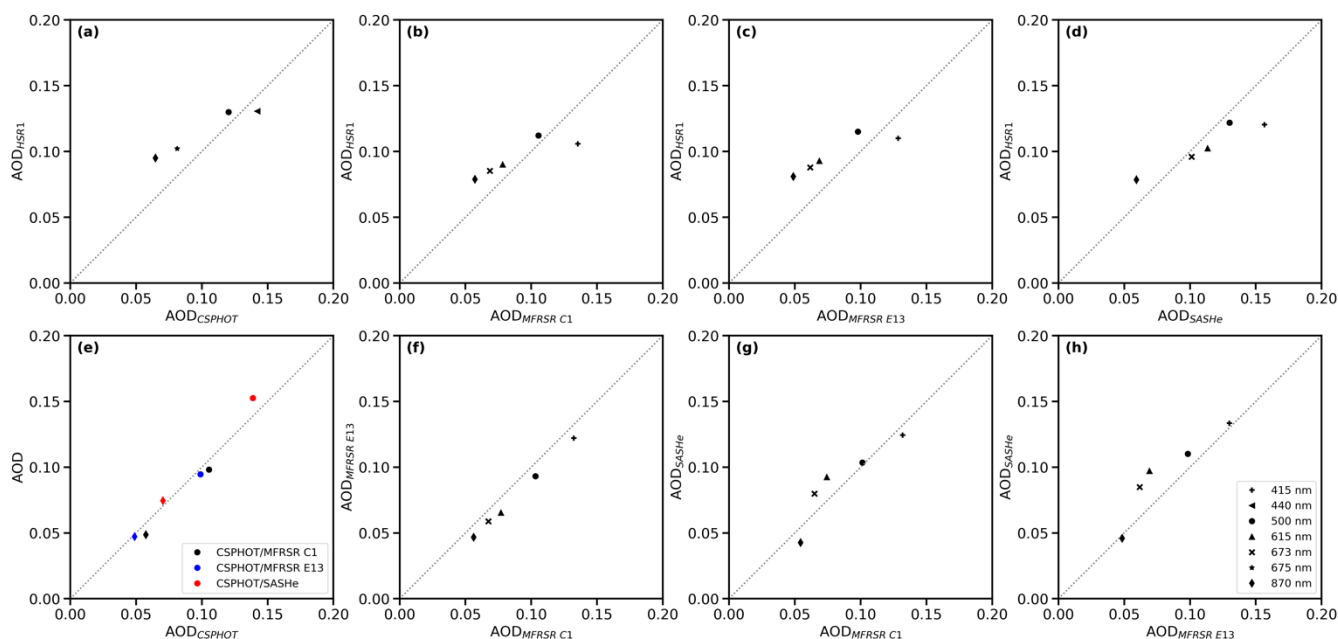
Figure 7: Mean spectral AOD (black) of collocated (a) CSPHOT and HSR1, (b) MFRSR C1 and HSR1, (c) MFRSR E13 and HSR1, (d) SASHe and HSR1, (f) MFRSR C1 and MFRSR E13, (g) MFRSR C1 and SASHe, and (h) MFRSR E13 and SASHe. Mean spectral AOD of collocated CSPHOT with MFRSR C1 (black), MFRSR E13 (blue), and SASHe (red) are shown in (e). The
400   **wavelengths considered include 415 (plus sign), 440 (left pointing triangle), 500 (circle), 615 (triangle), 673 (x-mark), 675 (star), and 870 (diamond) nm. The 1:1 line is indicated by the dotted gray line.**

4.3 Diffuse ratio comparison

4.3.1 Broadband diffuse ratio comparison

405   The HSR1 diffuse ratio is constructed by considering the diffuse irradiance and the total irradiance both integrated

from 400 to 1000 nm and then dividing the integrated diffuse irradiance by the integrated total irradiance. The HSR1

integrated diffuse ratios were collocated and compared to the broadband diffuse ratios from Radflux (Sect. 2.2.4). The

motivation of this comparison is to understand if the HSR1 integrated diffuse ratio captures the diffuse ratio in the absence of

Atmospheric
Measurement
Techniques
Discussions

a diffuse broadband irradiance observation (e.g., only total broadband SW measurements) despite measuring only a portion

410   of the solar spectral range.

The resultant diffuse ratio comparison is shown in Fig. 8. The HSR1 integrated diffuse ratio is found to typically be smaller than the broadband diffuse ratios. In terms of the mean diffuse ratio, the HSR1 diffuse ratio is smaller than the broadband diffuse ratio by 0.036 (8.5%) for all times (Fig. 8a) and 0.014 (7.8%) for clear-sky times (Fig. 8b). The diffuse ratio comparison is also separated into overcast and partial cloudy-skies (not shown) and the mean (relative) differences are

415   0.047 (-5.0%) and 0.043 (-11.6%), respectively. In general, the HSR1 integrated diffuse ratio is 12% smaller or less with closer agreement for clear-sky in absolute difference and overcast conditions in relative difference and worse agreement during the dominant mode of partial cloudy-skies, which accounts for ~60% of all times.

To gauge the impact of the diffuse ratio error in terms of the flux errors, the error in the broadband diffuse flux is considered by comparing the broadband total flux ($F_{broadband,total}$) and HSR1 integrated diffuse ratio (DR_{HSR1}) to the

420   broadband diffuse flux ($F_{broadband,diffuse}$):

$$F_{diffuse,error} = F_{broadband,total} \: x \: DR_{HSR1} - F_{broadband,diffuse} \: . \tag{6}$$

The resultant flux error is shown in Fig. 8c. The mean diffuse flux error is -16.7 and -7.9 W m^{-2} for all times and clear-sky times, respectively. Noting the measurement uncertainty of ±3% in the diffuse flux (Michalsky and Long, 2016), only 16.5% (all times) and 18.3% (clear-sky times) of the diffuse flux errors due to considering the HSR1 diffuse ratio are within

425   measurement uncertainty.
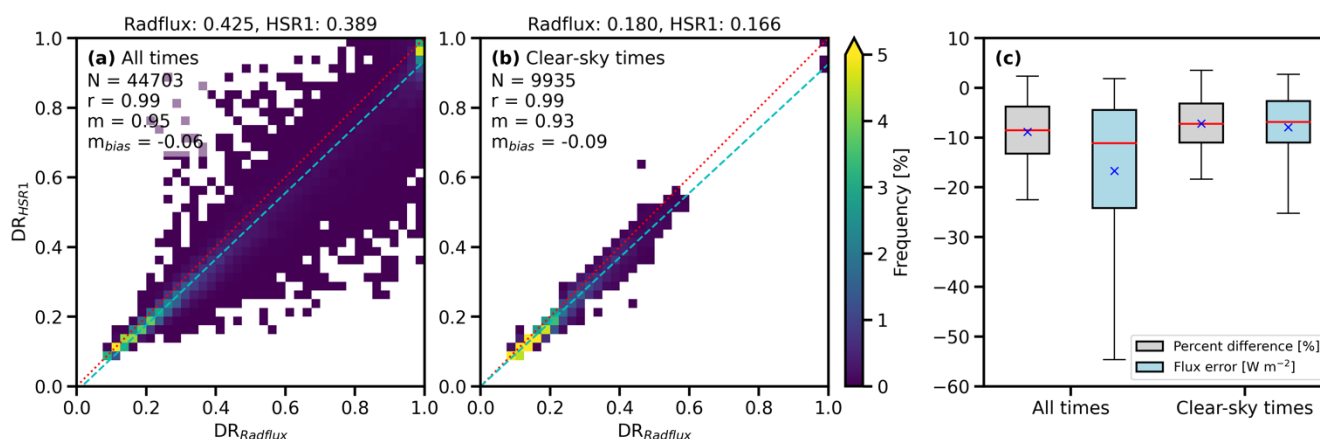
Figure 8: Frequency histogram for collocated diffuse ratio (DR) between Radflux and HSR1 for (a) all times, and (b) clear-sky times. The mean values are given above each plot and the sample size (N), correlation coefficient (r), slope of the regression line
430   **(m), and slope of the regression line of the bias (m$_{bias}$) are shown in the top left of each plot. The 1:1 line is indicated by the dotted red line and the regression line is indicated by the dashed light blue line. (c) Box plot of diffuse ratio percent difference (gray) between Radflux and HSR1 and flux error (light blue) in the broadband diffuse flux due to the HSR1 measured diffuse ratio. The whiskers of the box plot correspond to the 5th to 95th percentile. The mean value is denoted by a blue x-mark and the median is denoted by the red solid line.**

435

Atmospheric
Measurement
Techniques
Discussions
[EGU logo]
Open Access

4.3.2 Spectral diffuse ratio comparison

The HSR1 spectral diffuse ratios at 500 nm (i.e., $F_{diffuse, 500 nm}/F_{total, 500 nm}$) were compared to spectral diffuse ratios from the two MFRSRs in Fig. 9. The mean (relative) differences for the HSR1 spectral diffuse ratio at 500 nm compared to those from the MFRSR C1 and MFRSR E13 are -0.040 (-8.1%), and -0.042 (-8.4%). The correlation coefficients between

440   the HSR1 spectral diffuse ratio and those from the MFRSRs are 0.98 (MFRSR C1) and 0.97 (MFRSR E13). As expected, the spectral diffuse ratio comparison is similar to the total and diffuse spectral irradiance comparison. The diffuse ratio from the two MFRSRs were compared to each other as well with excellent agreement within 0.002 for the mean, which corresponds to 0.4% for the relative difference. Overall, the HSR1 spectral diffuse ratio is typically smaller than those from the two MFRSRs at 500 nm although general agreement is found with relative differences of 8%.

445
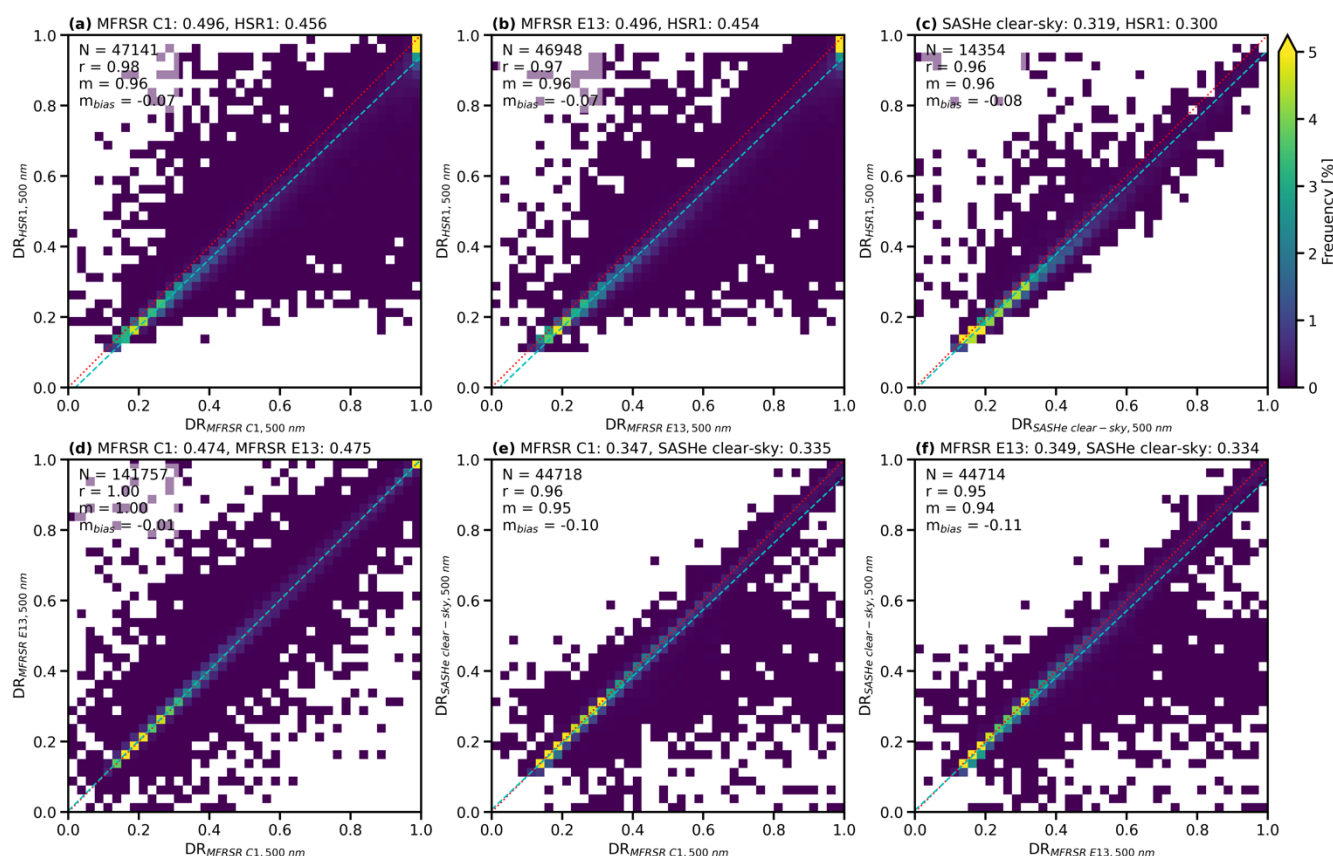
Figure 9: Frequency histogram for the diffuse ratio at 500 nm of collocated (a) MFRSR C1 and HSR1, (b) MFRSR E13 and HSR1, (c) SASHe and HSR1, (d) MFRSR C1 and MFRSR E13, (e) MFRSR C1 and SASHe, and (f) MFRSR E13 and SASHe. The mean values are given above each plot. The sample size (N), correlation coefficient (r), regression line slope (m), and bias regression line
450   **slope (m_{bias}) are shown in the top left of each plot. The 1:1 line is indicated by the dotted red line and the regression line is indicated by the dashed light blue line. Note that SASHe diffuse ratios are limited to clear-sky conditions.**

Atmospheric
Measurement
Techniques
Discussions

The HSR1 spectral diffuse ratios at 500 nm were also compared to the SASHe clear-sky diffuse ratios (Fig. 9c). The mean (relative) difference for the HSR1 spectral diffuse ratio at 500 nm compared to the SASHe diffuse ratio is -0.019 (-5.9%) with a correlation coefficient of 0.96. The SASHe clear-sky spectral diffuse ratios were also compared to those from the two MFRSRs. The mean (relative) differences for the SASHe diffuse ratios compared to those from the MFRSR C1 and MFRSR E13 are -0.012 (-3.6%), and -0.015 (-4.3%), respectively. The SASHe diffuse ratio at 500 nm comparisons are similar to the irradiance comparison in that the SASHe total spectral irradiances are similar in value to the HSR1 and MFRSR total irradiances but the HSR1 diffuse irradiance is smaller than the SASHe diffuse irradiance and the SASHe diffuse irradiance is smaller than those from the two MFRSRs.

The HSR1 spectral diffuse ratios were compared to spectral diffuse ratios from the two MFRSRs for MFRSR wavelengths (not shown). Similar to the spectral diffuse irradiance comparison at 500 nm (Fig. 3), the mean HSR1 spectral diffuse ratio is smaller than those from the two MFRSRs. For all times, the mean HSR1 spectral diffuse ratio is smaller than those from both MFRSRs by 0.05 (10%) or less at all wavelengths except for 940 nm where it is 0.06-0.08 (17-20%). The results are similar when considering clear-sky times: diffuse ratios are smaller by 0.05 or less with relative differences of 12% or less except at 940 nm where the relative difference is 32-42%. The range in the diffuse ratio percent differences are also similar across all wavelengths. For all times, the 5th to 95th percentile ranges from -28% to -10%. The exception is again at 940 nm where the diffuse ratio range nearly triples (i.e., -64% to -12%). The diffuse ratios from the two MFRSRs were also compared to each other, with the 5th to 95th percentile ranging from -5% to 12%, except for 940 nm where the range is -2% to 37%.

The SASHe clear-sky spectral diffuse ratios were also compared at 415, 615, 673, and 870 nm. The results are found to be similar to the 500 nm results. The HSR1 diffuse ratio is smaller than the SASHe diffuse ratio by 6% or less except at 870 nm where it is larger by 3% whereas the SASHe diffuse ratio is smaller than those from the two MFRSRs by 2 to 12%.

Interestingly, the spectral diffuse ratio comparison results are similar to those from the broadband diffuse ratio comparison (Fig. 8). This suggests that the biased low HSR1 diffuse measurements due to the instrument design may be the dominant feature that explains the difference in the broadband diffuse ratio and not that the HSR1 measures less of the solar spectrum than a broadband radiometer.

4.4 PAR comparison

The HSR1 PAR was compared to the PQS1 PAR in Fig. 10. The mean (relative) difference for the HSR1 PAR compared to the PQS1 PAR is 53.9 (4.7%) μmol m^{-2} s^{-1}. For PQS1 PAR values below ~1000 μmol m^{-2} s^{-1}, the collocated PAR observations with the highest frequency align along the 1:1 line with a mean difference of 45.7 μmol m^{-2} s^{-1}. Above ~1000 μmol m^{-2} s^{-1}, HSR1 PAR values are biased high with a deviation from the 1:1 line and a mean difference of 67.6 μmol m^{-2} s^{-1}. However, the largest disagreement values switch from biased high to biased low near values of about 1500 μmol m^{-2}

485   s^{-1}. This can be seen in that the 1st (99th) percentiles of the differences are -219.8 (807.7) µmol m^{-2} s^{-1} and -917.9 (326.1) µmol m^{-2} s^{-1} for values below and above 1500 µmol m^{-2} s^{-1}, respectively.

     The PAR comparison was separated into collocated times that are clear-sky, partial cloudy-sky, or overcast (not shown). The mean (relative) difference is 86.2 (6.0%), 64.3 (4.8%), and -4.9 (-1.0%) µmol m^{-2} s^{-1} for clear-sky, partial cloudy-sky, and overcast, respectively. Better agreement is found for overcast conditions and worse agreement is found for

490   clear-sky conditions. This aligns with the results presented in Fig. 10 such that better agreement is found at lower values than at higher values, where higher values correspond more towards clear-sky and lower values correspond more so to overcast conditions. While the mean difference is largest for clear-skies, the spread in the comparison is smallest noting that the correlation coefficient is highest (1.00) and the standard deviation of the difference (59.4 µmol m^{-2} s^{-1}) is the smallest of the three conditions. This may suggest that for clear-skies the conversion factor is too large or that the HSR1 total spectral

495   irradiance is consistently too high in this spectral range. The spread in the PAR comparison in Fig. 10 is largely due to partial cloudy-skies and overcast skies as the standard deviations of the differences are 210.3 and 129.6 µmol m^{-2} s^{-1}, respectively. The larger standard deviations may be partially a consequence of clouds rapidly varying over time and space.

     While the PQS1 is utilized as a reference PAR measurement to evaluate the HSR1 PAR, there is no reported uncertainty for the PQS1 PAR and no traceable accurate reference for PAR measurements. Across different PAR

500   instruments, the reported estimated PAR uncertainty is typically within 5% for ideal conditions but intercomparisons can be up to 20% different even for the same instrument (Mõttus et al., 2012). This suggests that the HSR1 PAR estimates are generally within measurement uncertainties of existing PAR instruments even under different conditions.
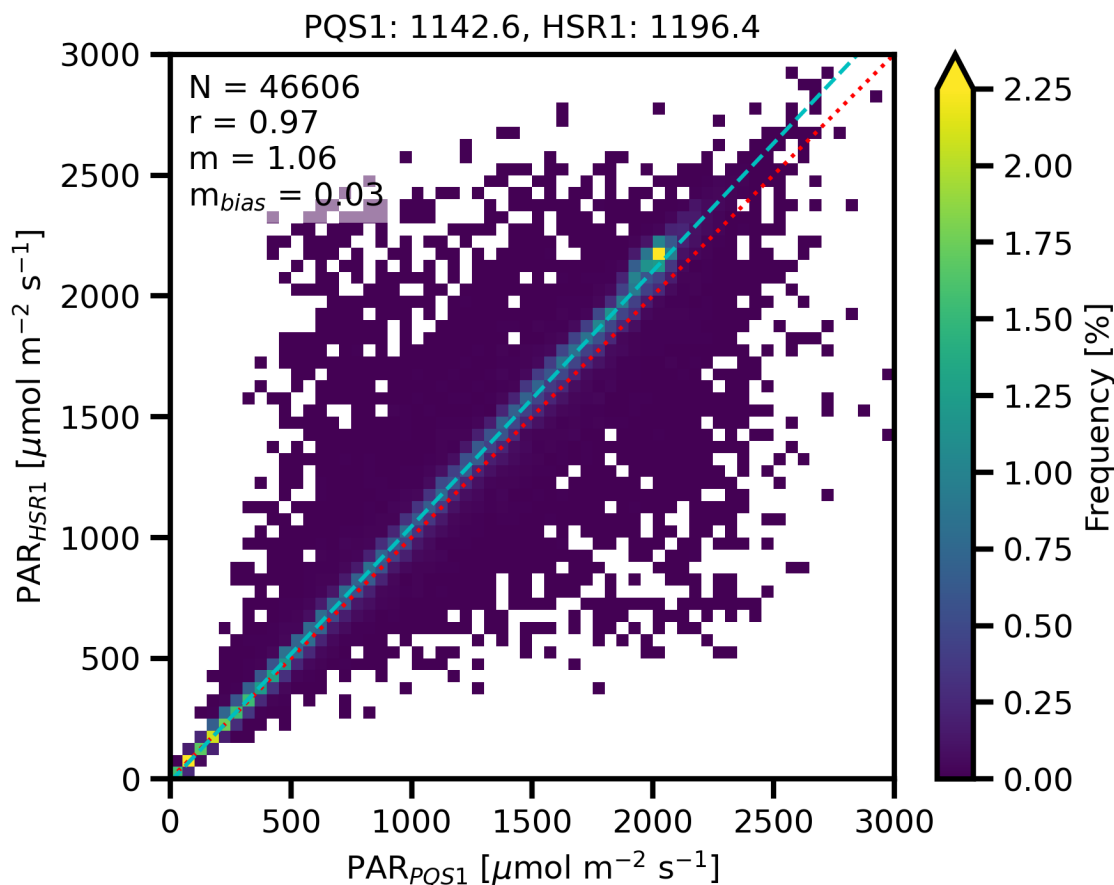
Figure 10: Frequency histogram for collocated PAR (µmol m^{-2} s^{-1}) between the PQS1 and the HSR1. The mean values are given above the plot and the sample size (N), correlation coefficient (r), regression line slope (m), and bias regression line slope (m$_{bias}$) are shown in the top left. The 1:1 line is indicated by the dotted red line and the regression line is indicated by the dashed light blue line.

5 Discussion

In this study, the HSR1 is evaluated for future use as a hyperspectral radiometer. We have presented and conducted the analysis using the HSR1 data that was processed in real-time and uploaded during the test period. Since the instrument deployment, several post-processing modifications and calibration checks have been tested. The post-processing modifications arise from issues noted in the data and attempting to correct the data for the known issues (e.g., dome lensing effect). The subsequent effects on the results are identified.

In general, the effects of the post-processing modifications on the results are small with a change of 0.01 or less in the total spectral irradiance, diffuse spectral irradiance, and spectral AOD at 500 nm (not shown). Our plan is to explore

potential post-processing modifications in a future study to identify potential improvements to the instrument's data and feasibility in implementation.

In addition, two calibration checks were tested. First, the Langley calibrations are compared to a reference TOA
520   spectral irradiance used in the SMARTS solar model (v2.9.5) (Gueymard, 2004). The initial comparison shows a wavelength offset of 5 nm, and an increasing intensity sensitivity of the HSR1 with increasing wavelength.

For the second calibration check, the HSR1 measured a 1kW 'FEL' filament lamp, with a calibrated intensity output certified by the UK NPL. This calibration check showed a high sensitivity of up to 5% in the 450 to 600 nm range, with lower errors at either end of the spectrum. Similar to the post-processing modifications, a detailed examination of calibration
525   checks and techniques will be reported in a future paper.

6 Summary

The HSR1 was tested at the ARM SGP site for two months. The HSR1 spectral irradiance measurements were compared to nearby collocated spectral radiometers including two MFRSRs and the SASHe. The HSR1 spectral AOD was also retrieved and compared to retrieved spectral AODs from nearby collocated instruments including those from the
530   CSPHOT, the MFRSRs, and the SASHe. Other quantities such as the diffuse ratio and PAR were also compared to collocated instruments.

The HSR1 total spectral irradiances were compared to the MFRSR C1 and MFRSR E13 total spectral irradiance. At 500 nm, the mean (relative) differences for the HSR1 total irradiance compared to the MFRSR C1 and MFRSR E13 total irradiances are 0.014 W m^{-2} nm^{-1} (1.5%) and 0.010 (1.1%) W m^{-2} nm^{-1} with correlation coefficients of 0.98. The comparison
535   indicates that the HSR1 total irradiance at 500 nm is slightly larger than those from both MFRSRs. However, the mean differences are small and when paired with the large correlation coefficients, demonstrates excellent agreement between the HSR1 total spectral irradiance and those from the two MFRSRs.

The HSR1 total spectral irradiances were also compared to the MFRSR C1 and MFRSR E13 total spectral irradiances for all MFRSR wavelengths (i.e., 415, 500, 615, 673, 870, and 940 nm). The results are similar to those at 500
540   nm such that the mean HSR1 total spectral irradiances values are slightly larger than the mean total spectral irradiances values from the MFRSRs. The exception is at 415 nm where the HSR1 total spectral irradiance is slightly smaller than those from the MFRSRs by ~2-3%. The relative differences between the HSR1 total spectral irradiance and those from the MFRSRs are 8% or less except at 940 nm where the HSR1 total spectral irradiance is larger than those from the MFRSRs by 16-20%.

545   The HSR1 diffuse spectral irradiances were compared to the two MFRSRs diffuse spectral irradiance. At 500 nm, the mean (relative) differences for the HSR1 diffuse spectral irradiance compared to the MFRSR C1 and MFRSR E13 diffuse spectral irradiance are -0.033 W m^{-2} nm^{-1} (-9.6%) and -0.036 (-10.4%) W m^{-2} nm^{-1} with correlation coefficients of 0.98. The HSR1 diffuse spectral irradiances are smaller than those from both MFRSRs, which may be partially related to the

underlying assumptions of isotropic diffuse radiation in the instrument design. Despite the consistently lower diffuse spectral

550   irradiance values, the relative differences are within about 10% with large correlation coefficients, which indicates good

agreement between the HSR1 diffuse spectral irradiances and those from the MFRSRs.

The HSR1 diffuse spectral irradiances were also compared to the MFRSR C1 and MFRSR E13 diffuse spectral irradiances for all MFRSR wavelengths. The HSR1 spectral diffuse irradiances are smaller than those from both the MFRSRs at all MFRSR wavelengths by ~4-14%.

555   The HSR1 spectral irradiances were also compared to SASHe irradiances, which were available only during clear-sky conditions. At 500 nm, the mean (relative) difference for the HSR1 irradiances compared to the SASHe irradiances is 0.017 W m^{-2} nm^{-1} (1.5%) for the total irradiance and -0.019 W m^{-2} nm^{-1} (-6.4%) for the diffuse irradiance. For other wavelengths, the total spectral irradiance comparisons are similar to those at 500 nm as the HSR1 total spectral irradiance is typically slightly larger than the SASHe total spectral irradiance by 0.08 W m^{-2} nm^{-1} (9%) or less except at 415 nm where the

560   HSR1 total spectral irradiance is smaller by 0.01 W m^{-2} nm^{-1} (1.5%). The HSR1 mean diffuse spectral irradiances are smaller than the SASHe diffuse spectral irradiances by 0.03 W m^{-2} nm^{-1} (9%) or less at other wavelengths compared.

The HSR1 clear-sky spectral AODs were compared to those from the CSPHOT, the MFRSRs, and the SASHe. At 500 nm, the mean (relative) differences for the HSR1 AOD compared to the CSPHOT, MFRSR C1, MFRSR E13, and SASHe AODs are 0.010 (8.0%), 0.007 (6.4%), 0.017 (17.7%), and -0.008 (-6.2%), respectively, with correlation coefficients

565   ranging between 0.91 to 0.94. In general, the HSR1 AOD is larger than those from the other instruments except for the SASHe AOD. The mean differences in AOD are 0.01 or less with less than 10% relative differences (except for the MFRSR E13), which demonstrates excellent agreement. Furthermore, the mean difference between the CSPHOT AOD and HSR1 AOD is within CSPHOT's uncertainty of 0.01.

The HSR1 clear-sky spectral AODs were compared to the CSPHOT, the two MFRSRs, and the SASHe AODs for

570   all overlapping wavelengths (i.e., 415, 440, 500, 615, 673, 675, and 870 nm). For the CSPHOT and MFRSR AODs comparison, the results are similar to those at 500 nm such that the HSR1 mean AOD is larger, except at 415 and 440 nm where the HSR1 AOD is smaller. For the SASHe AOD comparison, the HSR1 AOD is smaller at all wavelengths except at 870 nm where the HSR1 AOD is larger. Larger AOD disagreement relatively is found at higher wavelengths than at smaller wavelengths. Similar to the spectral irradiance comparison, better AOD agreement is found for the other instruments

575   compared to each other.

The HSR1 diffuse ratios were compared to the broadband diffuse ratios from Radflux and spectral diffuse ratios from the MFRSRs and SASHe. For the broadband comparison, the HSR1 mean integrated diffuse ratio is typically smaller than the broadband diffuse ratios by 0.036 (8.5%) for all times and 0.014 (7.8%) for clear-sky times. The agreement is worse for partial cloudy-skies (11.8%). For the spectral comparison, the mean (relative) diffuse ratio differences are ~-0.05 or less

580   (12% or less) for the MFRSR wavelengths except for the MFRSR diffuse ratio comparison at 940 nm where the relative difference is ~20-40%. The similarity between the broadband and spectral diffuse ratio comparison suggests that the

underestimation in the HSR1 diffuse spectral irradiance measurements is the likely source of the broadband disagreement more so than the HSR1 measuring a portion of the solar spectrum.

The HSR1 PAR was compared to the PQS1 PAR. The mean (relative) difference for the HSR1 PAR compared to the PQS1 PAR is 53.9 (4.7%) μmol m^{-2} s^{-1}. Better agreement is found for overcast conditions (-1.0%) and worse agreement is found for clear-sky conditions (6.0%). However, the spread in the PAR comparison is smallest for clear-sky, noting that the correlation coefficient is highest (1.00) and the standard deviation of the difference is smallest (59.4 μmol m^{-2} s^{-1}). The spread in the PAR comparison is largely due to partial cloudy-skies and overcast skies as the standard deviation of the differences are larger (~130-210 μmol m^{-2} s^{-1}). The larger spread for the cloudy-sky PAR comparison may be partially due to clouds rapidly varying over time and space.

7 Conclusion

A hyperspectral radiometer was evaluated in terms of operability and performance in measuring surface irradiances and aerosol optical properties. The analysis was limited to those two variables in this study due to the number of comparison data sources available, although retrievals of other atmospheric and land surface properties are possible with hyperspectral measurements. The scientific need for hyperspectral radiometers will continue to increase in importance in the future as weather, climate, and renewable energy forecasting advance to incorporate spectral characteristics of aerosols and clouds. With the advancement of hyperspectral radiometers to meet this need, increased knowledge and process understanding of the atmosphere are possible.

Data availability

Data can be downloaded from the ARM data archive (https://www.arm.gov/data/) for the HSR1 (sgphsr1C1.00; http://dx.doi.org/10.5439/1888171), CSPHOT (csphotaodfiltqav3; http://dx.doi.org/10.5439/1461660), MFRSR (sgpmfrsr7nchaod1michC1.c1 and sgpmfrsr7nchaod1michE13.c1; http://dx.doi.org/10.5439/1756632), ozone (gecomiX1.a1; http://dx.doi.org/10.5439/1874262), PAR (sgpco2flxrad4mC1.b1; http://dx.doi.org/10.5439/1313017), and Radflux (sgpradflux1longE13.c1; http://dx.doi.org/10.5439/1395157).

Author contribution

KAB, LDR, JW, CF, AT, and MR conceptualized the study. JW provided the HSR1 instrument and data. JW, AT, and MR provided project administration that facilitated the instrument deployment. CF, LM, GBH, and CH facilitated the operation and data processing of the comparison instruments. KAB and JW performed the formal analysis. KAB drafted the manuscript and prepared the figures. KAB, LDR, JW, CF, AT, LM, GBH, and CH reviewed and edited the manuscript.

Competing interests

The authors declare that they have no conflict of interest.

Acknowledgements

References

Alexandrov, M. D., Lacis, A. A., Carlson, B. E., and Cairns, B.: Remote sensing of atmospheric aerosols and trace gases by means of multifilter rotating shadowband radiometer. Part II: Climatological applications, J. Atmos. Sci., 59, 544–566, https://doi.org/10.1175/1520-0469(2002)059<0544:rsoaaa>2.0.co;2, 2002.

Alexandrov, M. D., Lacis, A. A., Carlson, B. E., and Cairns, B.: Remote sensing of atmospheric aerosols and trace gases by means of multifilter rotating shadowband radiometer. Part I: Retrieval algorithm, J. Atmos. Sci., 59, 524–543, https://doi.org/10.1175/1520-0469(2002)059<0524:rsoaaa>2.0.co;2, 2002.

Atmospheric Radiation Measurement (ARM) user facility: Sunphotometer (CSPHOTAODFILTQAV3). 2022-05-16 to 2022-07-18, Southern Great Plains (SGP) Central Facility, Lamont, OK (C1). Compiled by L. Gregory and C. Sivaraman. ARM Data Center. Data set accessed 2022-10-17 at http://dx.doi.org/10.5439/1461660. 1994.

Atmospheric Radiation Measurement (ARM) user facility: Ozone Monitoring Instrument (OMI). 2022-05-16 to 2022-07-18, Global Earth Coverage (GEC) External Data (satellites and others) (X1). Compiled by B. Ermold. ARM Data Center. Data set accessed 2022-09-07 at http://dx.doi.org/10.5439/1874262. 2004.

Atmospheric Radiation Measurement (ARM) user facility: Carbon Dioxide Flux Measurement Systems (CO2FLXRAD4M). 2022-05-16 to 2022-07-18, Southern Great Plains (SGP) Central Facility, Lamont, OK (C1). Compiled by A. Koontz and S. Biraud. ARM Data Center. Data set accessed 2022-08-18 at http://dx.doi.org/10.5439/1313017. 2016.

Atmospheric Radiation Measurement (ARM) user facility: Radiative Flux Analysis (RADFLUX1LONG). 2022-05-15 to 2022-07-18, Southern Great Plains (SGP) Lamont, OK (Extended and Co-located with C1) (E13). Compiled by L. Riihimaki. ARM Data Center. Data set accessed 2022-09-01 at http://dx.doi.org/10.5439/1395159. 2020.

Atmospheric Radiation Measurement (ARM) user facility: Aerosol Optical Depth (AOD)

640   derived from MFRSR measurements (MFRSR7NCHAOD1MICH). 2022-05-15 to 2022-07-18, Southern Great
           Plains (SGP) Central Facility, Lamont, OK (C1). Compiled by T. Shippert. ARM Data Center. Data set accessed
           2022-09-01 at http://dx.doi.org/10.5439/1756632. 2021.

Atmospheric Radiation Measurement (ARM) user facility: Aerosol Optical Depth (AOD)
           derived from MFRSR measurements (MFRSR7NCHAOD1MICH). 2022-05-15 to 2022-07-18, Southern Great
645   Plains (SGP) Lamont, OK (Extended and Co-located with C1) (E13). Compiled by T. Shippert. ARM Data Center.
           Data set accessed 2022-12-09 at http://dx.doi.org/10.5439/1756632. 2021.

Atmospheric Radiation Measurement (ARM) user facility: hyperspectral radiometer (HSR1). 2022-05-15 to 2022-07-
           17, Southern Great Plains (SGP) Central Facility, Lamont, OK (C1). ARM Data Center. Data set accessed 2022-07-
           17 at http://dx.doi.org/10.5439/1888171. 2022.

650 Badosa, J., Wood, J., Blanc, P., Long, C. N., Vuilleumier, L., Demengel, D., and Haeffelin, M.: Solar irradiances measured
           using SPN1 radiometers: Uncertainties and clues for development, Atmos. Meas. Tech., 7, 4267–4283,
           https://doi.org/10.5194/AMT-7-4267-2014, 2014.

Chan, S. W., and S. C. Biraud: Carbon Dioxide Flux Measurement System (CO2FLX) Instrument Handbook. Ed. by
           Robert Stafford, U.S. Department of Energy. DOE/SC-ARM/TR-048. https://doi.org/10.2172/1020279. 2022.

655 Delia García-Cabrera, R., Cuevas-Agulló, E., Barreto, Á., Eugenia Cachorro, V., Pó, M., Ramos, R., and Hoogendijk, K.:
           Aerosol retrievals from the EKO MS-711 spectral direct irradiance measurements and corrections of the
           circumsolar radiation, Atmos. Meas. Tech., 13, 2601–2621, https://doi.org/10.5194/AMT-13-2601-2020, 2020.

Ermold, B., C. J. Flynn, and J. Barnard: Aerosol Optical Depth Value-Added Product for the SAS-He Instrument,
           Version 1.0. U.S. DOE, Office of Science, Office of Biological and Environmental Research. DOE/SC-ARM/TR-
660   133. https://doi.org/10.2172/1226568. 2013.

Flynn, C. J.: Shortwave Array Spectroradiometer–Hemispheric (SASHe) Instrument Handbook. Ed. by Robert
           Stafford, DOE ARM Climate Research Facility. DOE/SC-ARM-TR-172. https://doi.org/10.2172/1251414. 2016.

Giles, D. M., Sinyuk, A., Sorokin, M. G., Schafer, J. S., Smirnov, A., Slutsker, I., Eck, T. F., Holben, B. N., Lewis, J. R.,
           Campbell, J. R., Welton, E. J., Korkin, S. V., and Lyapustin, A. I.: Advancements in the Aerosol Robotic Network
665   (AERONET) Version 3 database - automated near-real-time quality control algorithm with improved cloud
           screening for Sun photometer aerosol optical depth (AOD) measurements, Atmos. Meas. Tech., 12, 169–209,
           https://doi.org/10.5194/amt-12-169-2019, 2019.

Gueymard, C. A.: The sun's total and spectral irradiance for solar energy applications and solar radiation models, Sol.
           Energy, 76, 423–453, https://doi.org/10.1016/J.SOLENER.2003.08.039, 2004.

670 Hansen, J. E. and Travis, L. D.: Light scattering in planetary atmospheres, Space Sci. Rev., 16, 527–610,
           https://doi.org/10.1007/BF00168069, 1974.

Harrison, L., Beauharnois, M., Berndt, J., Kiedron, P., Michalsky, J., and Min, Q.: The rotating shadowband

spectroradiometer (RSS) at SGP, Geophys. Res. Lett., 26, 1715–1718, https://doi.org/10.1029/1999GL900328, 1999.

675 Harrison, L., Michalsky, J., and Berndt, J.: Automated multifilter rotating shadow-band radiometer: an instrument for optical depth and radiation measurements, Appl. Opt., 33, 5118–5125, https://doi.org/10.1364/AO.33.005118, 1994.

Hodges, G. B., and J. J. Michalsky: Multifilter Rotating Shadowband Radiometer (MFRSR), Multifilter Radiometer (MFR), and Normal Incidence Multifilter Radiometer (NIMFR) Instrument Handbook. Ed. by Robert Stafford, DOE ARM Climate Research Facility. DOE/SC-ARM-TR-144. https://doi.org/10.2172/1251387. 2016.

680 Holben, B. N., Eck, T. F., Slutsker, I., Tanré, D., Buis, J. P., Setzer, A., Vermote, E., Reagan, J. A., Kaufman, Y. J., Nakajima, T., Lavenu, F., Jankowiak, I., and Smirnov, A.: AERONET—A Federated Instrument Network and Data Archive for Aerosol Characterization, Remote Sens. Environ., 66, 1–16, https://doi.org/10.1016/S0034-4257(98)00031-5, 1998.

Kasten, F. and Young, A. T.: Revised optical air mass tables and approximation formula, Appl. Opt., 28, 4735–4738,
685 https://doi.org/10.1364/AO.28.004735, 1989.

Koontz, A., G. Hodges, J. Barnard, C. Flynn, and J. Michalsky: Aerosol Optical Depth Value-Added Product Report. U.S. Department of Energy. DOE/SC-ARM/TR-129. https://doi.org/10.2172/1092419. 2013.

Levelt, P. F., Joiner, J., Tamminen, J., Veefkind, J. P., Bhartia, P. K., Zweers, D. C. S., Duncan, B. N., Streets, D. G., Eskes, H., Van Der, R. A., McLinden, C., Fioletov, V., Carn, S., De Laat, J., Deland, M., Marchenko, S., McPeters, R.,
690 Ziemke, J., Fu, D., Liu, X., Pickering, K., Apituley, A., Abad, G. G., Arola, A., Boersma, F., Miller, C. C., Chance, K., De Graaf, M., Hakkarainen, J., Hassinen, S., Ialongo, I., Kleipool, Q., Krotkov, N., Li, C., Lamsal, L., Newman, P., Nowlan, C., Suleiman, R., Tilstra, L. G., Torres, O., Wang, H., and Wargan, K.: The Ozone Monitoring Instrument: Overview of 14 years in space, Atmos. Chem. Phys., 18, 5699–5745, https://doi.org/10.5194/ACP-18-5699-2018, 2018.

695 Li, Z., Moreau, L., and Cihlar, J.: Estimation of photosynthetically active radiation absorbed at the surface, J. Geophys. Res. Atmos., 102, 29717–29727, https://doi.org/10.1029/97JD01219, 1997.

Long, C. N. and Ackerman, T. P.: Identification of clear skies from broadband pyranometer measurements and calculation of downwelling shortwave cloud effects, J. Geophys. Res. Atmos., 105, 15609–15626, https://doi.org/10.1029/2000JD900077, 2000.

700 Long, C. N., Ackerman, T. P., Gaustad, K. L., and Cole, J. N. S.: Estimation of fractional sky cover from broadband shortwave radiometer measurements, J. Geophys. Res. Atmos., 111, 11204, https://doi.org/10.1029/2005JD006475, 2006.

McComiskey, A. and Ferrare, R. A.: Aerosol Physical and Optical Properties and Processes in the ARM Program, Meteorol. Monogr., 57, 21.1-21.17, https://doi.org/10.1175/AMSMONOGRAPHS-D-15-0028.1, 2016.

705 Michalsky, J. J., Liljegren, J. C., and Harrison, L. C.: A comparison of Sun photometer derivations of total column water

vapor and ozone to standard measures of same at the Southern Great Plains Atmospheric Radiation Measurement site, J. Geophys. Res. Atmos., 100, 25995–26003, https://doi.org/10.1029/95JD02706, 1995.

Michalsky, J. J. and Long, C. N.: ARM Solar and Infrared Broadband and Filter Radiometry, Meteorol. Monogr., 57, 16.1-16.15, https://doi.org/10.1175/AMSMONOGRAPHS-D-15-0031.1, 2016.

710   Michalsky, J. and Harrison, L.: Objective algorithms for the retrieval of optical depths from ground-based measurements, Appl. Opt., 33, 5126–5132, https://doi.org/10.1364/AO.33.005126, 1994.

Min, Q., Wang, T., Long, C. N., and Duan, M.: Estimating fractional sky cover from spectral measurements, J. Geophys. Res. Atmos., 113, https://doi.org/10.1029/2008JD010278, 2008.

Mõttus, M., Sulev, M., Baret, F., Lopez-Lozano, R., and Reinart, A.: Photosynthetically Active Radiation: Measurement and
715   Modeling, Encycl. Sustain. Sci. Technol., 7902–7932, https://doi.org/10.1007/978-1-4419-0851-3_451, 2012.

Norgren, M. S., Wood, J., Sebastian Schmidt, K., Van Diedenhoven, B., Stamnes, S. A., Ziemba, L. D., Crosbie, E. C., Shook, M. A., Scott Kittelman, A., Leblanc, S. E., Broccardo, S., Freitag, S., and Reid, J. S.: Above-aircraft cirrus cloud and aerosol optical depth from hyperspectral irradiances measured by a total-diffuse radiometer, Atmos. Meas. Tech., 15, 1373–1394, https://doi.org/10.5194/AMT-15-1373-2022, 2022.

720   Riihimaki LD, KL Gaustad, and CN Long: Radiative Flux Analysis (RADFLUXANAL) Value-Added Product: Retrieval of Clear-Sky Broadband Radiative Fluxes and Other Derived Values. Ed. by Robert Stafford, ARM user facility. DOE/SC-ARM-TR-228. https://doi.org/10.2172/1569477. 2019.

Riihimaki, L. D., Flynn, C., McComiskey, A., Lubin, D., Blanchard, Y., Chiu, J. C., Feingold, G., Feldman, D. R., Gristey, J. J., Herrera, C., Hodges, G., Kassianov, E., LeBlanc, S. E., Marshak, A., Michalsky, J. J., Pilewskie, P., Schmidt, S.,
725   Scott, R. C., Shea, Y., Thome, K., Wagener, R., and Wielicki, B.: The Shortwave Spectral Radiometer for Atmospheric Science: Capabilities and Applications from the ARM User Facility, Bull. Am. Meteorol. Soc., 102, E539–E554, https://doi.org/10.1175/BAMS-D-19-0227.1, 2021.

Turner, D. D., Mlawer, E. J., and Revercomb, H. E.: Water Vapor Observations in the ARM Program, Meteorol. Monogr., 57, 13.1-13.18, https://doi.org/10.1175/AMSMONOGRAPHS-D-15-0025.1, 2016.

730   Wang, T. and Min, Q.: Retrieving optical depths of optically thin and mixed-phase clouds from MFRSR measurements, J. Geophys. Res. Atmos., 113, 19203, https://doi.org/10.1029/2008JD009958, 2008.

Wood, J. G.: Solar radiation sensor, Patent WO 99/13359, 26 pp. 1999.

Wood, J., Smyth, T. J., and Estellés, V.: Autonomous marine hyperspectral radiometers for determining solar irradiances and aerosol optical properties, Atmos. Meas. Tech., 10, 1723–1737, https://doi.org/10.5194/AMT-10-1723-2017, 2017.